February 6, 2007 (submitted to ApJ November 10, 2006)

STELLAR EVOLUTIONARY EFFECTS ON THE ABUNDANCE OF PAHS AND SN-CONDENSED DUST IN GALAXIES

Frédéric Galliano, Eli Dwek

Observational Cosmology Lab., Code 665, NASA Goddard Space Flight Center, Greenbelt MD 20771, USA

galliano@milkyway.gsfc.nasa.gov

and

Pierre Chanial

Astrophysics Group, Blackett Laboratory, Imperial College, Prince Consort Road, London SW7 2AZ, UK

ABSTRACT

Spectral and photometric observations of nearby galaxies show a correlation between the strength of their mid-IR aromatic features and their metal abundance, and a deficiency of these features in low-metallicity galaxies. The aromatic features are most commonly attributed to emission from PAH molecules. In this paper, we suggest that the observed correlation represents a trend of PAH abundance with galactic age, reflecting the delayed injection of PAHs and carbon dust into the ISM, by AGB stars in their final, post-AGB phase of their evolution. These AGB stars are the primary sources of PAHs and carbon dust in galaxies, and recycle their ejecta back to the interstellar medium only after a few hundred million years of evolution on the main sequence. In contrast, more massive stars that explode as Type II supernovae inject their metals and dust almost instantaneously after their formation. After determining the PAH abundances in 35 nearby galaxies, we use a chemical evolution model to show that the delayed injection of carbon dust by AGB stars provides a natural explanation to the dependence of the PAH content in galaxies with metallicity. We also show that larger dust particles giving rise to the far-IR emission follow a distinct evolutionary trend closely related to the injection of dust by massive stars into the ISM.

Subject headings: ISM: dust – infrared: galaxies – galaxies: starburst – galaxies: evolution – stars: post-AGB – supernovae remnants

1. INTRODUCTION

Spectral and photometric observations of nearby galaxies with the *Infrared Space Observatory* (*ISO*) and the *Spitzer Space Telescope* have provided the opportunity to investigate the inter-relations between global galactic properties, such as morphology, star formation activity, spectral energy distribution (SED), metallicity, and dust abundance and composition. In particular, these observations have enabled detailed studies of the correlation of dust abundances and composition with metal enrichment in galaxies spanning a wide range of metallicities. Since the metallicity of galaxies evolves monotonically with time, galaxies with different metallicities provide snapshots of the evolutionary history of galaxies.

An exciting result provided by *ISO* spectral observations of nearby galaxies was the discovery of a striking correlation between the strength of their mid-IR aromatic features and their metallicity (Madden et al. 2006). Low-metallicity galaxies exhibited very weak or no aromatic features. Observations of the 8-to-24 μm bands flux ratio obtained with *Spitzer*/IRAC and *Spitzer*/MIPS instruments showed a correlation of this flux ratio with the galaxies' oxygen abundance (Engelbracht et al. 2005). Since the *Spitzer*/IRAC$_{8\mu m}$ band is supposed to trace the strength of the aromatic features, and the *Spitzer*/MIPS$_{24\mu m}$ that of the continuum emission from the hot non-aromatic dust component, this correlation seemed to confirm the trends discovered by *ISO*. This correlation was independently confirmed by Wu et al. (2006) and O'Halloran et al. (2006) from spectral observations of low-metallicity blue compact dwarf galaxies with the *Spitzer*/IRS instrument.

The aromatic features are most commonly attributed to the vibrational modes of Polycyclic Aromatic Hydrocarbons (PAHs; Léger & Puget 1984; Allamandola et al. 1985), which are large planar molecules made of 50 to 1000 carbon atoms. Their ubiquity makes them an important component of dust models (Désert et al. 1990; Dwek et al. 1997; Draine & Li 2001; Li & Draine 2001; Zubko et al. 2004), locking up $\sim 15 - 20\%$ of the total amount of interstellar carbon (Zubko et al. 2004, with solar abundance constraints). They mostly reside in galactic photodissociation regions (PDRs), where they play an important role in the heating of the gas by providing photo-electrons (e.g. Tielens & Hollenbach 1985; Bakes & Tielens 1994), and in interstellar chemistry by providing surfaces for chemical reactions. Because of their small sizes, PAHs are stochastically heated by the interstellar radiation fields. The relative strength of some of the aromatic features depends on their ionization state, and varies therefore significantly with the physical condition of the environment (Hony et al.

2001; Vermeij et al. 2002; Galliano et al. 2007). Understanding the evolution of PAHs and their relation to the global properties of galaxies is therefore extremely important because of the complex mutual influences between PAHs, and their ambient radiative and gaseous surroundings.

Several explanations have been offered for the correlation of the intensity of the PAH features with metallicity. The first suggests that the trend reflects an increase in the destruction efficiency of PAHs in low metallicity environments Galliano et al. (2003, 2005); Madden et al. (2006). Low-metallicity environments are bathed with harder photons than our Galaxy, due to the higher effective temperature of their stars, and their young age. Moreover, the paucity of dust allows this hard radiation field to penetrate deeper into the ISM, compared to high-metallicity systems, selectively destroying the PAH molecules by photoevaporation or photodissociation. **This explanation is consistent with the models of population synthesis and dust evolution of Dwek et al. (2000). Assuming that PAHs are efficiently destroyed by UV photons in H II regions, their models showed an evolutionary trend of PAH features with time, as the relative contribution of ionizing OB stars to the galaxy's SED decreases with time.** A second explanation has been proposed by O'Halloran et al. (2006), who suggested that PAHs are destroyed by the numerous shocks observed in low metallicity systems. To support their proposition, they showed an anti-correlation between the PAH-to-continuum ratio and the $[\mathrm{Fe\,II}]_{25.99\mu m}/[\mathrm{Ne\,II}]_{12.81\mu m}$ line ratio, the latter being supposedly a shock tracer. The problem with this explanation is that there is no observational evidence that PAHs are selectively destroyed in shocks. On the contrary, Reach et al. (2002) showed that, in the shocked medium of 3C 391, both the PAH features and the underlying continuum disappear.

All previous explanations attribute the paucity of PAHs to destructive processes that are more efficient in the early stages of galaxy evolution. In contrast, Dwek (2005) suggested that the observed correlation reflects an evolutionary trend of the sources of interstellar PAHs with metallicity. PAHs and carbon dust are mostly produced in asymptotic giant branch (AGB) stars which, unlike massive stars, recycle their ejecta into the ISM after a significantly longer time of main sequence evolution. The observed correlation of PAH line intensities with metallicity is therefore a trend of PAH abundance with galactic age, reflecting the delayed injection of PAHs and carbon dust into the ISM by AGB stars in their final, post-AGB, phase of their evolution.

Such distinct evolutionary trends of SN and AGB produced dust with time were predicted by Dwek (1998) and more recently by Morgan & Edmunds (2003). In particular, the latter show the evolutionary trend of AGB dust with time. This trend can be translated as a trend with metallicity if galaxies approximately share

a global "cosmic" star formation history.

The goal of this paper is to present a detailed evolutionary model to examine whether the observed trend of PAH line intensity with metallicity reflects an evolutionary trend of PAH abundance with metallicity. This requires the determination of PAH abundance from the strength of their aromatic features in the galaxies for which this trend has been observed, and the use of a chemical evolution model to follow the change of PAH abundance with galactic metallicity (Dwek 1998). The paper is organized as follows. We first present in Sect. 2 the sample of nearby galaxies that were considered in our analysis. In Sect. 3, we describe the method we used to determine the intrinsic stellar radiation field, and the abundance of PAHs as well as the larger grains in these galaxies. In Sect. 4, we briefly describe the chemical evolution model used in the calculations, and compare its results to the abundances derived from our SED modeling. The results of the paper are briefly summarized in Sect. 5.

Throughout this paper we will refer to the solar abundances by Grevesse & Sauval (1998), the oxygen number abundance being $12 + \log(\mathrm{O/H})_\odot = 8.83$, the Helium and heavy elements to gas mass ratios $Y_\odot = 0.248$ and $Z_\odot = 0.017$, respectively. Besides, we assume that the helium abundance is independent of the metallicity.

2. THE SAMPLE OF NEARBY GALAXIES

2.1. Source Selection

In order to properly characterize the PAH emission, we considered galaxies whose mid-IR spectrum has been observed, either with one of the spectrographs onboard the *ISO* satellite, or with the *Spitzer*/IRS. We combined ISO samples of starbursts and AGNs (Laurent et al. 2000), spirals (Roussel et al. 2001), ellipticals (Xilouris et al. 2004), dwarf galaxies (Madden et al. 2006), and the low-metallicity sources of the *Spitzer* sample presented by Engelbracht et al. (2005) which were observed by *Spitzer*/IRS. Among the ellipticals, only NGC 1399 has a mid-IR spectrum. Consequently, our sample includes various types of galaxies and covers a wide range of metallicities and star formation activity (Table 1).

The modeling that will be presented in §3 requires the assembly of data covering the stellar as well as the dust emission components, for each galaxy. First, we need most of the U, B, V, R, I, J, H, K fluxes, to constrain the stellar spectrum shape. Photometric J, H and K bands are available for almost all of our sources, thanks to the 2MASS survey (Jarrett et al. 2003). We rejected the galaxies Arp 118, Arp 236, Arp 299 and NGC 4038, for which no B and V bands were reported. Second, the far-IR SED is used to constrain the intensity of the interstellar radiation field (ISRF). Hence, we rejected galaxies which

have not been detected by IRAS or MIPS, such as HS 0822+3542, Tol 1214-277 and Tol 65. In addition, our mass estimates are normalised to the H I mass. We therefore rejected the galaxy IRAS 23128-5919, for which no H I observation was reported. Finally, we removed M 31 from our sample, since its angular diameter is too large to build a consistent observed total SED.

The global properties of the selected sources are presented in Table 1. If relevant, the distances were homogenised to $H_0 = 71\ \mathrm{km\,s^{-1}\,Mpc^{-1}}$. The masses have been scaled to the adopted distance.

Table 1. Select properties of the sample.

Name	R.A. (J2000)	Dec. (J2000)	Mid-IR spectrograph	Distance (Mpc)	$12+\log(\mathrm{O/H})$	[ref.]	$M_{\mathrm{H\,I}}$ ($10^8\ M_\odot$)	[ref.]	$M_{\mathrm{H_2}}$ ($10^8\ M_\odot$)	[ref.]	Notes
) 11	$00^h36^m52^s.5$	$-33°33'19''$	*Spitzer*/IRS	92	7.9	[2]	$\lesssim 1^{(?)}$	[2]	$\lesssim 1$	[2]	Pec H II
) 253	$00^h47^m32^s.9$	$-25°17'18''$	*ISO*/CAM	3.3	9.0	[3]	18	[4]	17	[5]	H II
) 520	$01^h24^m34^s.9$	$+03°47'31''$	*ISO*/CAM	27	(?)		35	[6]	35	[7]	Pec H II
) 613	$01^h34^m17^s.5$	$-29°24'58''$	*ISO*/CAM	19	9.2	[8]	37	[9]	···		Sy
) 891	$02^h22^m33^s.4$	$+42°20'57''$	*ISO*/CAM	9.6	8.9	[10]	76	[9]	49	[9]	Edge-on
) 1068	$02^h42^m40^s.6$	$-00°00'47''$	*ISO*/CAM	15	9.0	[11]	22	[12]	74	[13]	Sy
) 1097	$02^h46^m19^s.1$	$-30°16'28''$	*ISO*/CAM	12	9.0	[14]	51	[15]	$\gtrsim 7.3$	[16]	Sy
) 1140	$02^h54^m33^s.5$	$-10°01'44''$	*ISO*/CAM	25	8.0	[17]	52	[18]	···		Irr H II
) 1365	$03^h33^m35^s.6$	$-36°08'23''$	*ISO*/CAM	19	9.1	[19]	130	[20]	170	[21]	Sy
0335-052	$03^h37^m44^s.0$	$-05°02'38''$	*Spitzer*/IRS	54	7.3	[22]	9.9	[23]	···		BCD
) 1399	$03^h38^m29^s.1$	$-35°27'03''$	*ISO*/CAM	21	(?)		$\lesssim 2$	[9]	···		cD
42	$03^h46^m49^s.7$	$+68°05'45''$	*ISO*/CAM	3.8	8.9	[24]	130	[9]	50	[9]	H II
) 1569	$04^h30^m49^s.1$	$+64°50'52''$	*ISO*/CAM	2.2	8.2	[25]	1.3	[26]	0.50	[27]	Irr H II
) 1808	$05^h07^m42^s.3$	$-37°30'47''$	*ISO*/CAM	11	9.1	[28]	18	[29]	20	[30]	Sy
w 40	$05^h55^m42^s.7$	$+03°23'29''$	*ISO*/CAM	10	8.1	[31]	4.2	[9]	0.23	[9]	BCD
)-10	$08^h36^m15^s.2$	$-26°24'34''$	*Spitzer*/IRS	8.7	8.9	[25]	3.1	[32]	1.6	[32]	Irr H II
r 18	$09^h34^m02^s.0$	$+55°14'28''$	*Spitzer*/IRS	13	7.2	[22]	1.2	[33]	···		BCD
2	$09^h55^m51^s.8$	$+69°40'46''$	*ISO*/CAM	3.6	9.0	[34]	9.0	[35]	13	[36]	Irr H II
) 3256	$10^h27^m51^s.1$	$-43°54'17''$	*ISO*/CAM	37	8.9	[37]	62	[38]	300	[39]	Pec H II
: 33	$10^h32^m31^s.9$	$+54°24'04''$	*Spitzer*/IRS	20	8.4	[37]	4.3	[40]	0.70	[41]	Irr H II
: 153	$10^h49^m05^s.0$	$+52°20'08''$	*Spitzer*/IRS	37	7.8	[42]	6.7	[43]	···		BCD
Zw 403	$11^h27^m59^s.9$	$+78°59'39''$	*Spitzer*/IRS	4.5	7.7	[22]	0.69	[40]	···		BCD
448	$11^h42^m12^s.4$	$+00°20'03''$	*Spitzer*/IRS	70	8.0	[44]	47	[45]	24	[45]	Pec H II
) 4945	$13^h05^m26^s.2$	$-49°28'15''$	*ISO*/CAM	3.9	(?)		45	[46]	17	[47]	Edge-on S
taurus A	$13^h25^m28^s.0$	$-43°01'06''$	*ISO*/CAM	3.8	~ 9	[48]	11	[49]	2.0	[50]	Elliptical S
1	$13^h29^m52^s.7$	$+47°11'43''$	*ISO*/CAM	8.4	8.7	[51]	50	[52]	56	[53]	
3	$13^h37^m00^s.7$	$-29°51'58''$	*ISO*/CAM	4.5	9.2	[54]	51	[55]	49	[56]	H II

Table 1—Continued

Name	R.A. (J2000)	Dec. (J2000)	Mid-IR spectrograph	Distance (Mpc)	$12 + \log(O/H)$	[ref.]	$M_{H\,I}$ ($10^8\ M_\odot$)	[ref.]	M_{H_2} ($10^8\ M_\odot$)	[ref.]	Notes
l 89	$14^h01^m21^s.5$	$-33°03'50''$	*Spitzer*/IRS	15	8.0	[57]	13	[58]	···		H II
rcinus	$14^h13^m09^s.6$	$-65°20'21''$	*ISO*/CAM	4.0	(?)		55	[46]	11	[59]	Sy
3C 5253	$13^h39^m55^s.7$	$-31°38'29''$	*ISO*/SWS	3.3	8.2	[17]	0.91	[60]	$\lesssim 0.1$	[61]	Irr H II
p 220	$15^h34^m57^s.2$	$+23°30'11''$	*ISO*/CAM	73	(?)		280	[38]	160	[62]	ULIRG
3C 6240	$16^h52^m58^s.8$	$+02°24'06''$	*ISO*/CAM	98	(?)		88	[9]	310	[9]	LIRG
3C 6946	$20^h34^m51^s.2$	$+60°09'17''$	*ISO*/CAM	5.5	9.1	[63]	56	[64]	33	[65]	H II
k 930	$23^h31^m58^s.3$	$+28°56'50''$	*Spitzer*/IRS	73	8.1	[44]	28	[66]	···		H II
3C 7714	$23^h36^m14^s.1$	$+02°09'19''$	*Spitzer*/IRS	37	8.5	[67]	17	[68]	22	[68]	Pec H II

eferences. — [2] Bergvall et al. (2000); [3] Zaritsky et al. (1994); [4] Boomsma et al. (2005); [5] Houghton et al. (1997); [6] Bernloehr 3); [7] Yun & Hibbard (2001); [8] Alloin et al. (1979); [9] Bettoni et al. (2003); [10] Otte et al. (2001); [11] Dutil & Roy (1999); Staveley-Smith & Davies (1987); [13] Helfer et al. (2003); [14] Storchi-Bergmann et al. (1995); [15] Ondrechen & van der Hulst (1989); Gerin et al. (1988); [17] Heckman et al. (1998); [18] Hunter et al. (1994); [19] Roy & Walsh (1997); [20] Jorsater & van Moorsel (1995); Sandqvist et al. (1995); [22] Izotov et al. (1999); [23] Thuan et al. (1999a); [24] Pilyugin et al. (2004); [25] Kobulnicky & Skillman 7); [26] Stil & Israel (2002); [27] Israel (1997); [28] Ravindranath & Prabhu (2001); [29] Dahlem et al. (2001); [30] Dahlem et al. 0); [31] Pérez-Montero & Díaz (2003); [32] Sauvage et al. (1997); [33] van Zee et al. (1998); [34] Boselli et al. (2002); [35] Appleton . (1981); [36] Walter et al. (2002); [37] Mas-Hesse & Kunth (1999); [38] Casasola et al. (2004); [39] Sargent et al. (1989); [40] Thuan . (2004); [41] Israel (2005); [42] Kunth & Joubert (1985); [43] Thuan & Martin (1981); [44] Izotov & Thuan (1998); [45] Sage et al. 2); [46] Huchtmeier & Richter (1988); [47] Dahlem et al. (1993); [48] Schaerer et al. (2000); [49] Richter et al. (1994); [50] Wild . (1997); [51] Bresolin et al. (2004); [52] Dean & Davies (1975); [53] Helfer et al. (2003); [54] Webster & Smith (1983); [55] Tilanus len (1993); [56] Lundgren et al. (2004); [57] Durret et al. (1985); [58] Paturel et al. (2003); [59] Elmouttie et al. (1998); [60] Reif . (1982); [61] Meier et al. (2002); [62] Sanders et al. (1991); [63] Kobulnicky et al. (1999); [64] Carignan et al. (1990); [65] Tacconi ung (1986); [66] Hopkins et al. (2002); [67] Gonzalez-Delgado et al. (1995); [68] Struck & Smith (2003).

te. — The sources are ordered according to their right ascension. The symbol (?) identifies uncertain values. Entries for the

allicity for which no data exist are marked by $\cdots$, and assumed to be solar-to-supersolar. The H_2 masses are not used to calculate dust-to-gas mass ratio, because the IR emission was assumed to originate entirely from the H I gas.

2.2. *ISO*/CAM Data Reduction

Most of the sources in Table 1 were observed with *ISO*/CAM (Cesarsky et al. 1996a) on board the *ISO* satellite (Kessler et al. 1996). These spectra were used by Madden et al. (2006), and we refer to this work for a detailed description of the data reduction. The CVF performed spectral imaging using a 32×32 detector array, with a sampling of $3''$pixel^{-1} or $6''$pixel^{-1} in our cases, from $\lambda = 5$ μm to 16.5 μm with one pointing of two CVFs, from $\lambda = 5$ to 9.5 μm and from $\lambda = 9.0$ to 16.5 μm. The spectral resolution goes from $\lambda/\Delta\lambda = 35$ to 51 across the full spectra.

For the data treatment, we used the CAM Interactive Reduction (CIR, version AUG01; Chanial 2003). The subtraction of the dark currents was performed using the Biviano et al. (1998) model which predicts the time evolution for each row of the detector, taking into account drifts along each orbit and each revolution. We masked the glitches using multi-resolution median filtering (Starck et al. 1999) on each block of data after slicing the cube. Additional deglitching was performed manually, examining the temporal cut for each pixel. We corrected the systematic memory effects using the Fouks-Schubert method (Coulais & Abergel 2000). We computed a hybrid flat-field image placing a mask on the source and computing a flat field outside this mask from the median of the temporal cut for each pixel. For the pixels which were on-source, the flat-field response was set to the corresponding calibration flat-field. The conversion from Analog Digital Units to mJy/pixel was performed using the standard in-flight calibration data base. To remove the sky contribution, the sources smaller than the array were masked and, for a given wavelength, the median of the pixels which are off-source were subtracted from each pixel. For the more extended sources, we subtracted an independently observed zodiacal spectrum. The intensity of this spectrum was a free parameter varied in order to match the properly sky subtracted fluxes in the LW2 (6.7 μm) and LW3 (14.3 μm) broadbands. The final product is a 3D spectral-image of each galaxy. We integrated the spectrum into an aperture encompassing the entire galaxy, and to obtain the global SED of the galaxy. When the angular size of the source was larger than the one of the array, we scaled-up the spectrum to match the $IRAS_{12\mu m}$ broadband flux.

2.3. *Spitzer*/IRS Spectrum Extraction

Several of the low-metallicity sources in Table 1 were not observed by *ISO*/CAM, we therefore complemented our database with publically released mid-IR spectra from the *Spitzer*/IRS spectrometer on board the *Spitzer Space Telescope* (Houck et al. 2004b; Werner et al. 2004). Among these galaxies, the spectra of SBS 0335-052, NGC 7714, VII Zw 403, Haro 11 and I Zw 18 are described in details in Houck et al. (2004a), Brandl et al. (2004) and

Wu et al. (2006). We considered only low-resolution data, taken with the SL (Short-Low) module, from $\lambda = 5.2$ μm to 14.5 μm, and the LL (Long-Low) module, from $\lambda = 14.0$ μm to 38.0 μm, both with a spectral resolution of $\lambda/\Delta\lambda \simeq 64 - 128$.

. We retrieved the Basic Calibrated Data (BCD) that have been preprocessed by the Spitzer Science Center (SSC) data reduction pipeline, and converted to flux density, corrected for stray light and flatfielded. The extraction of the spectra from the 2D space/wavelength images was performed with the Spectral Modeling, Analysis and Reduction Tool (SMART, version 5.5.6; Higdon et al. 2004). We first inspected the BCD images and identified the hot pixels which have not been masked out by the SSC. We replaced them by the median of their neighbors. For each module, an off-source position is observed. We subtracted this spectrum from the on-source one, in order to remove the sky emission. The extraction of the 1D spectrum was performed inside a column whose width vary with the wavelength. We have excluded the bonus order. Then, the various frames, for each nod position, were coadded. Since the long wavelength end of the SL module and the short wavelength end of the LL one were not systematically overlapping, we finally scaled the SL module, in order to obtain a continuous spectrum. This scaling factor can be as large as 50%. At the time when this publication is written, the *Spitzer*/IRS data handbook recommends not to derive the signal-to-noise ratio from the uncertainties generated by the pipeline. Instead of that, we adopted the recommended systematic error of 20%. However, the SL module of the noisiest spectra (VII Zw 403, Mrk 153, Mrk 930, I Zw 18, Tol 89) exhibits fluctuations larger than this value. To take into account these statistical variations, we smoothed these spectra into a $\Delta\lambda \simeq 0.2$ μm window (4 points), and took the standard deviation inside this window as the error. Similarly to what we did with *ISO*/CAM spectra (§2.2), in order to compensate the fact that we may be overlooking some extended emission, we scaled-up the *Spitzer*/IRS SL and LL spectra to match the $IRAS_{12\mu m}$ and $IRAS_{25\mu m}$. In the case of II Zw 40, the *Spitzer*/IRS spectrum does not exhibit the PAH features that Madden et al. (2006) detected in the extended emission, thus we prefer to use the *ISO*/CAM data for this galaxy. For Tol 89, the *Spitzer*/$IRAC_{8\mu m}$ broadband flux is higher than the integrated spectrum into the same band. This is probably due to the fact that the slit of *Spitzer*/IRS measures only the nucleus emission, which likely has a steeper continuum and weaker features than the extended emission contributing to the total broadband. Therefore, we will consider the mass of PAHs derived for this galaxy to be a lower limit.

2.4. The Multiwavelength SEDs

The UV-to-FIR SED of each galaxy was built using data from different catalogs. We extensively used the HYPERLEDA and NED databases. Most of the SEDs include *IRAS* broadband fluxes at 12, 25, 60 and 100 μm (Moshir & et al. 1990; Rice et al. 1988), and J, H, K 2MASS fluxes (Jarrett et al. 2003). For some of the galaxies, we completed the IR SED with the broadband *Spitzer* data reported by Dale et al. (2005). We kept only data encompassing the entire galaxy. The optical data were corrected for Galactic extinction, using the Schlegel et al. (1998) extinction maps.

For NGC 5253, we used the *ISO*/SWS observations of Crowther et al. (1999) to model the spectrum of this galaxy.

3. DETERMINATION OF THE GLOBAL MASS OF PAHS

3.1. Motivations and Approach

The 8/24 μm flux ratio provides information on the strength of the PAH features in the galaxy, although it is relatively limited. Indeed, the *Spitzer*/IRAC$_{8\mu m}$ flux is dominated by the 8.6 μm PAH feature, but can be dominated by the continuum, in the case of low-metallicity galaxies (Madden et al. 2006), or by the silicate extinction feature at 9.7 μm, in the case of deeply embedded sources (e.g. Spoon et al. 2004; Gallais et al. 2004). When there are no PAHs and the 8 μm is dominated by the continuum, the 8/24 μm ratio reflects the color of the mid-IR emitting silicates and graphites. The *Spitzer*/MIPS$_{24\mu m}$ flux is dominated by the continuum emission from the silicate and carbon grains. However, this part of the SED is very sensitive to the abundance of small grains (e.g. Galliano et al. 2003, 2005), and can originate additionally from large grains close to strong sources of radiation (e.g. Plante & Sauvage 2002; Vanzi & Sauvage 2004). Fig. 1 shows the ratio of the two bands, for the sources presented in Table 1. The error bars on the ratio, in Fig. 1, come from the propagation of the observational errors. The error bars on the metallicity were not systematically given by the authors who published them. An error of 0.1 dex in the O/H number abundance accounts for the typical dispersion between independent measurements. There were 6 sources, in Table 1, for which no metallicity measurements were reported. However, all of them have the morphology, optical colors, IR emission and H_2 content of solar or supersolar systems, with NGC 1399 probably having the largest metallicity. We assign an arbitrary $Z = (2 \pm 1)\ Z_\odot$ to these galaxies, and consider them to be uncertain.

The optical properties of the PAHs have not the same spectral shape than the ones

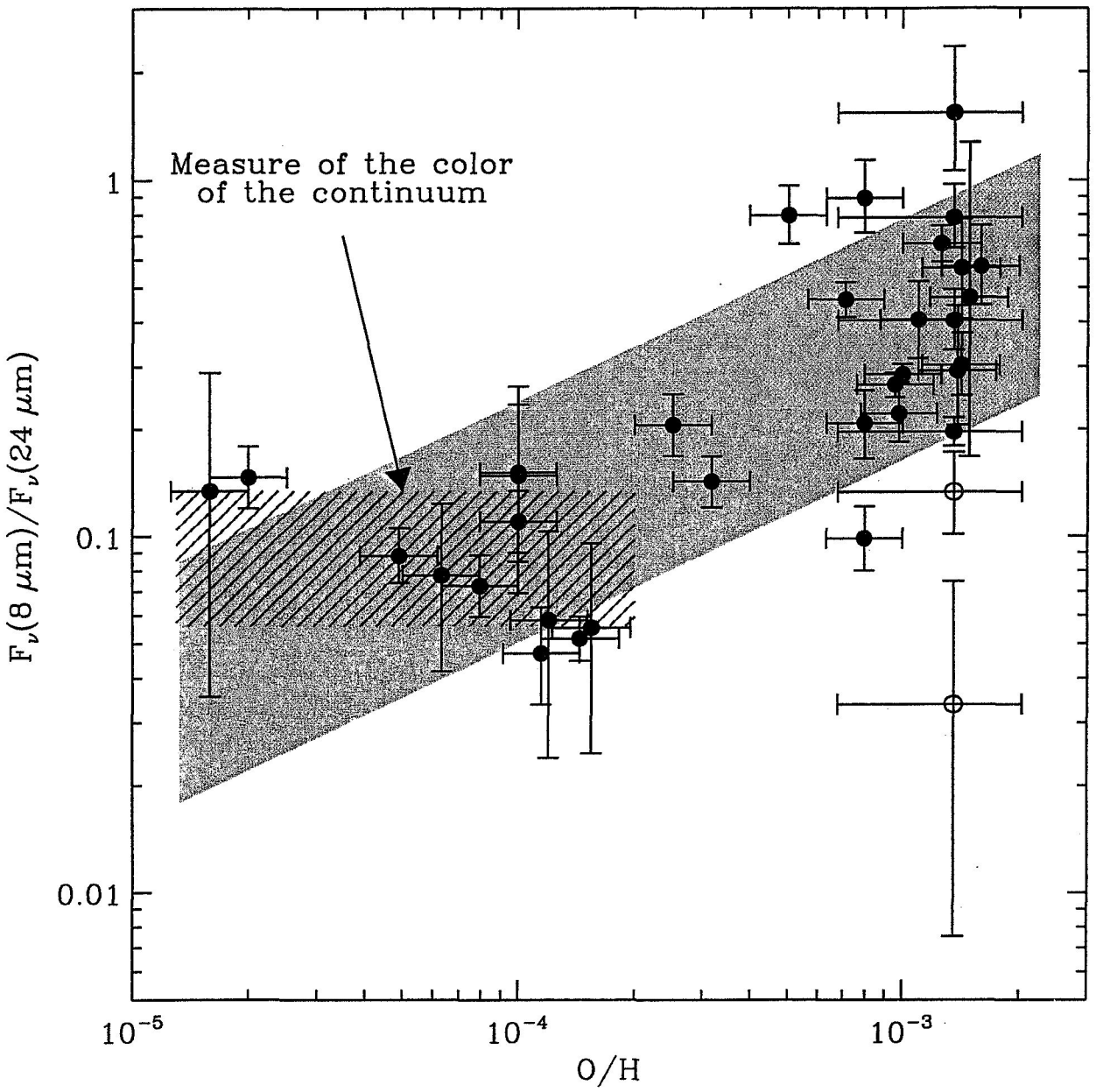

Fig. 1.— Mid-IR color as a function of the oxygen number abundance, for the sample in Table 1. Our observed SEDs have been integrated over the *Spitzer*/IRAC$_{8\mu m}$ and *Spitzer*/MIPS$_{24\mu m}$ bandpasses, in order to produce this plot. The two open circles are the (U)LIRGs of our sample. The grey stripe is the $\pm 1\sigma$ linear correlation between log(O/H) and $\log\left(F_\nu(8\ \mu m)/F_\nu(24\ \mu m)\right)$. The hatched stripe shows the range of the ratio ($0.06 \lesssim F_\nu(8\ \mu m)/F_\nu(24\ \mu m) \lesssim 0.13$), when it measures the color of the silicate and graphite continuum due to the weakness of the PAH features.

of solid-state grains (carbonaceous or silicates) believed to be the carriers of the mid-IR continuum. Fig. 2 shows the wavelength-dependence of the mass absorption coefficient, $\kappa_{\rm abs}$, of various types of grains. It shows that the value of $\kappa_{\rm abs}$ for PAHs drops by 4 orders of magnitude between 0.1 and 1 μm, where the stars emit most of their energy, while the $\kappa_{\rm abs}$ of graphite and silicate dust drop by less than 2 orders of magnitude. However, most of the energy is absorbed at shorter wavelengths. Thus, the PAHs are more sensitive to very young stellar populations than the grains responsible for the 24 μm continuum (Fig. 3), and a correct determination of their excitation rate should ideally take into account this property. Beyond 1 μm, the opacity of analog PAHs measured in laboratory (Mattioda et al. 2005) can be higher than the values stated by Li & Draine (2001).

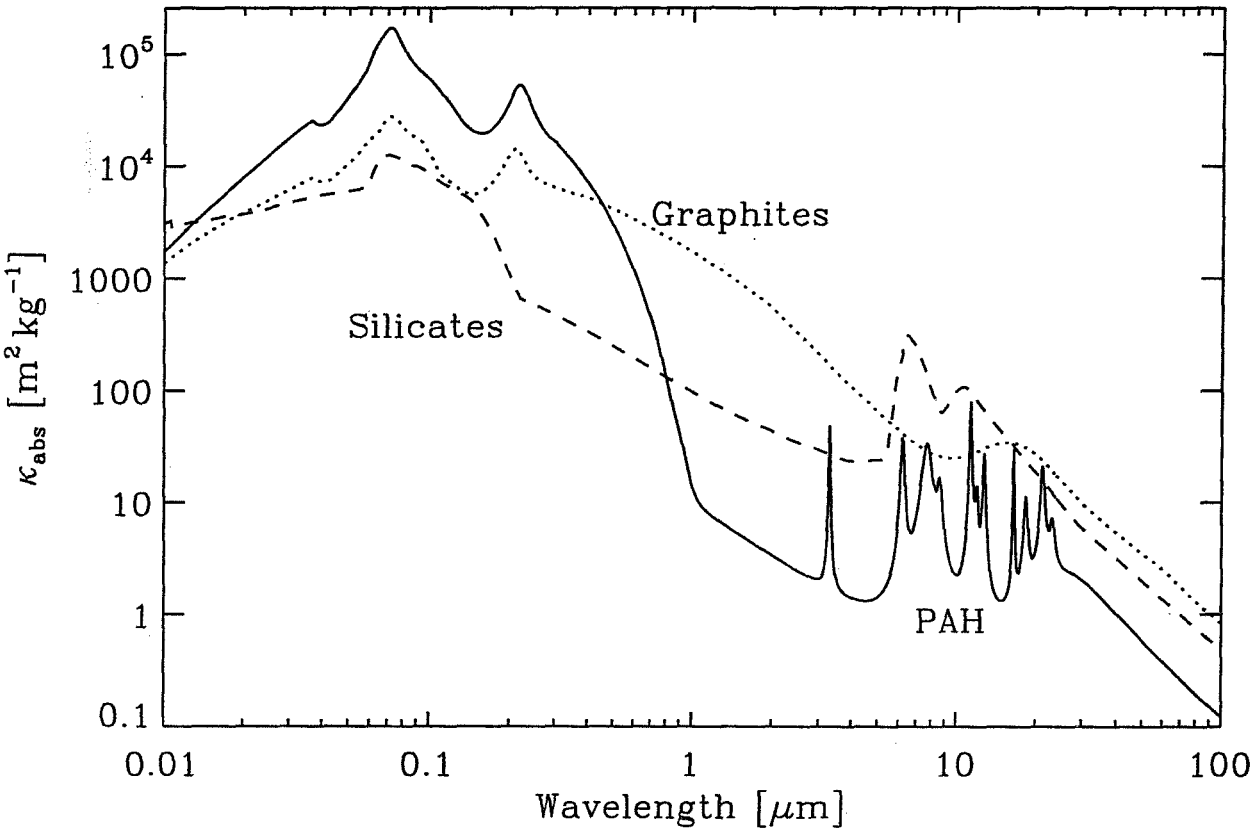

Fig. 2.— The wavelength-dependence of the mass absorption coefficient of the PAHs (Li & Draine 2001), graphites (Laor & Draine 1993) and silicates (Weingartner & Draine 2001), integrated over the Zubko et al. (2004) size distribution, for the bare grain model with solar abundance constraints (BARE-GR-S).

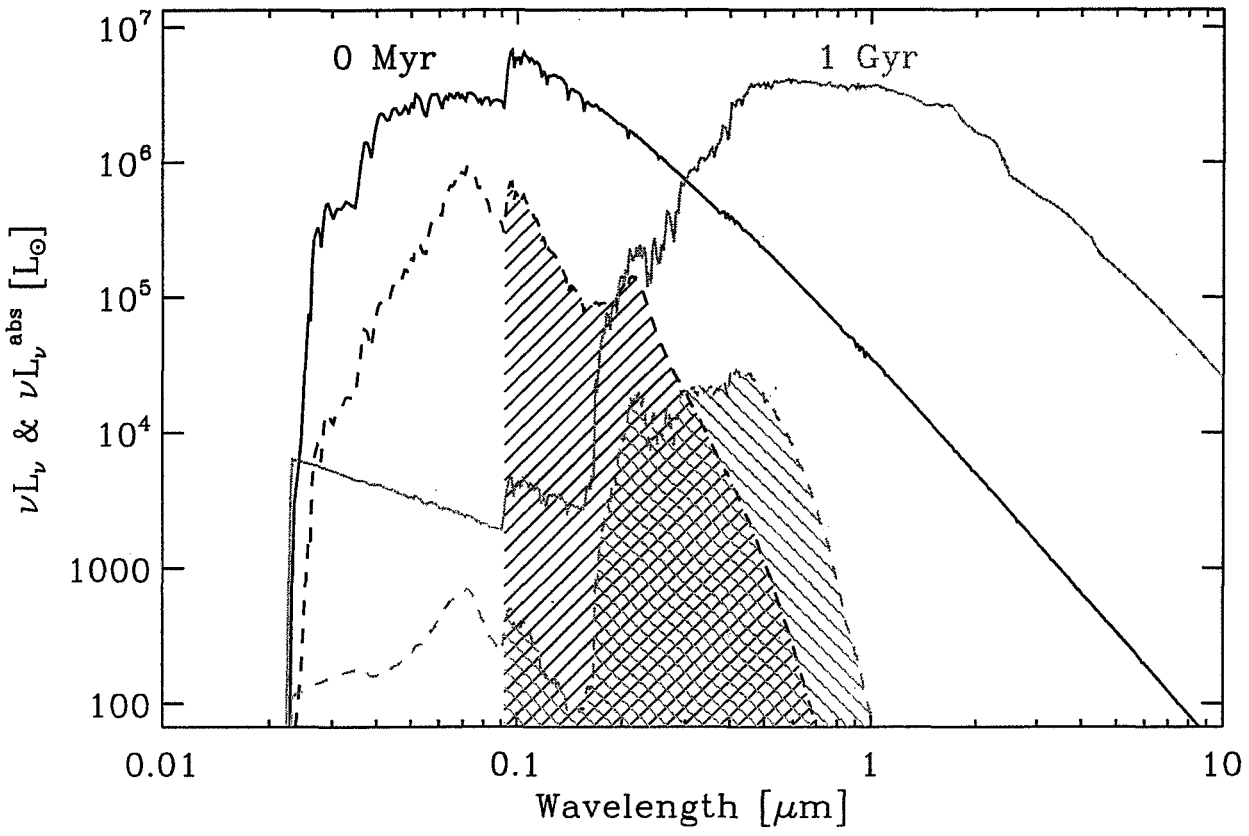

Fig. 3.— Sensitivity of the energy absorbed by the PAHs to the age of the stellar populations. The solid lines are two instantaneous bursts modeled with PÉGASE, with a Salpeter IMF. The black spectrum is taken immediately after the burst, while the grey one has evolved during 1 Gyr. The dashed lines are the part of these spectra absorbed by the PAHs, with the mass absorption coefficient of Fig. 2, and a thin slab geometry. The hatched areas are the energies carried by non-ionizing photons absorbed by the PAHs, for each stellar spectrum. This energy is 10 times higher for the young burst, than for the old one.

The determination of the mass of PAHs, from an observed SED, requires a more sophisticated approach than a simple modified black body fit, since they are transiently heated, hence only a fraction of them is excited at a given time. Consequently, a proper determination of the PAH content must also take into account the characteristics of the intrinsic radiation field, in addition to their size distribution.

3.2. Determination of the Global Interstellar Radiation Field

In order to study the variations of the PAH content with the metallicity, we considered several galaxies at different metallicities, some of these galaxies being scarcely observed. Thus, we developed a simple self-consistent model, fully constrained by the data. The major assumption of our approach is that the PAHs are bathed by an homogeneous radiation field throughout the galaxy. More precisely, we assume that PAHs are not present in H II regions, where they are destroyed (e.g. Cesarsky et al. 1996b; Peeters et al. 2002; Martín-Hernández et al. 2002), and that they are not present in molecular clouds, where they are probably accreted onto larger grains. **In star forming regions, the gas density to radiation field intensity is generally such that the H I/H_2 transition lies very close to the surface and that the gas in the UV penetrated cloud layer is partially molecular. However, most of the molecular mass is devoid of PAH emission.** We therefore assume that all the PAHs are associated with the H I gas, and that they do not receive any ionizing photons ($\lambda < 0.0912\ \mu m$), which are absorbed into the H II regions. Finally, we assume that the grains emitting most of the far-IR energy are bathed by the same radiation field as the PAHs. This latter assumption is corroborated in part by the observed correlation between the intensity of the PAH 7.7 μm feature and the 850 μm flux in galaxies (Haas et al. 2002). However, this correlation may not be valid at spatial resolutions high enough to resolve the clumps.

The determination of the intensity of the ISRF is done in the following steps.

Determination of the intrinsic stellar luminosity. We use the stellar evolution and population synthesis model PÉGASE (Fioc & Rocca-Volmerange 1997), in order to generate a proper stellar spectrum, for each galaxy. Its luminosity, $L^\star_\nu$, is the linear combination of two instantaneous bursts, of different ages. The stellar monochromatic luminosity is:

$$L^\star_\nu = M^\star_{\rm young} \times L^\dagger_\nu(t_{\rm young}) + M^\star_{\rm old} \times L^\dagger_\nu(t_{\rm old}), \quad (1)$$

$M^\star_{\rm old}$ and $M^\star_{\rm young}$ being the masses of each components, and $t_{\rm old}$ and $t_{\rm young}$ their ages. These are the free parameters. $L^\dagger_\nu(t)$ is the luminosity per unit mass, t Myr after

an instantaneous burst, assuming a Salpeter initial mass function. These two bursts represent the old underlying stellar population and the most recently formed one, respectively. This modeling does not take into account a possible contribution from an AGN, since in most of our galaxies, the SED is dominated by the stellar input.

Estimation of the escaping stellar light fraction. The escaping stellar radiation is:

$$L_\nu^{\text{UV-opt.}} = L_\nu^\star \times \mathcal{P}_{\text{esc}}(\tau, \omega), \tag{2}$$

where $\tau(\nu)$ is the optical depth of the medium and $\omega(\nu)$ the albedo of the dust. The escaping fraction, $\mathcal{P}_{\text{esc}}$, depends on the geometry of the medium. We consider consecutively two extreme geometries: a sphere where stars and dust are uniformly mixed (Városi & Dwek 1999):

$$\mathcal{P}_{\text{esc}}(\tau, \omega) = \frac{P_{\text{e}}(\tau)}{1 - \omega[1 - P_{\text{e}}(\tau)]}, \tag{3}$$

with

$$P_{\text{e}}(\tau) = \frac{3}{4\tau}\left[1 - \frac{1}{2\tau^2} + \left(\frac{1}{\tau} + \frac{1}{2\tau^2}\right) e^{-2\tau}\right]; \tag{4}$$

and a thin shell geometry with central illumination, for which:

$$\mathcal{P}_{\text{esc}}(\tau, \omega) = e^{-\tau}. \tag{5}$$

Another unknown is the shape of the extinction law, $\tau(\nu)$, and its corresponding albedo, $\omega(\nu)$. In order to avoid strong hypothesis on the dust properties, we consider consecutively Galactic, LMC and SMC extinction curves. Similarly to what Pei (1992) did, we fit these three curves with a linear combination of graphites and silicates, the PAHs representing only a small fraction of the mass are neglected at this point. We adopt the BARE-GR-S grain size distribution (bare grains with solar depletion constrains on the amount of metals locked into the dust; Zubko et al. 2004). The opacity of the grains is:

$$\kappa_{\text{dust}}(\nu) = \zeta_{\text{gra}} \times \kappa_{\text{gra}}(\nu) + \zeta_{\text{sil}} \times \kappa_{\text{sil}}(\nu), \tag{6}$$

where $\kappa_{\text{gra}}(\nu)$ and $\kappa_{\text{sil}}(\nu)$ are plotted at Fig. 2, and their derived relative mass fraction, ζ_{gra} and ζ_{sil}, are given in Table 2. For an homogeneous medium, with a dust mass density of ρ_{dust}:

$$\tau(\nu) = \kappa_{\text{dust}}(\nu) \times \int_0^L \rho_{\text{dust}}\, \mathrm{d}s \tag{7}$$

$$= \kappa_{\text{dust}}(\nu) \times \Lambda, \tag{8}$$

where L is the line of sight and Λ is the dust mass column density. Thus, for a given extinction type and geometry, the only free parameter governing $\mathcal{P}_{\text{esc}}(\tau, \omega)$ is Λ. The

Table 2: Mass fractions of silicate and graphite, for different extinction curves.

	Galaxy	LMC	SMC
$\zeta_{\rm d}^{\rm gra}$	0.36	0.14	0.02
$\zeta_{\rm d}^{\rm sil}$	0.64	0.86	0.98

escaping luminosity, $L_\nu^{\text{UV-opt.}}$, is constrained by the observed UV-optical broadband fluxes.

Derivation of the intrinsic radiation density. The intrinsic stellar monochromatic luminosity gives us the global shape of the ISRF. The radiation energy density, $\mathcal{U}_\nu$, is defined as follows:

$$L_\nu^\star(\nu) \times [1 - \mathcal{P}_{\rm esc}(\tau, \omega)] = c \iiint_V \rho_{\rm dust}(\vec{r}) \kappa_{\rm dust}(\nu) \times \mathcal{U}_\nu(\vec{r}, \nu)\, {\rm d}^3 r. \tag{9}$$

The left-hand side is the global absorbed energy, and the right-hand side is the integral over the volume of the locally absorbed energy. In the case of an homogeneous distribution, it gives:

$$\mathcal{U}_\nu(\nu) = \frac{1 - \mathcal{P}_{\rm esc}(\tau, \omega)}{c\, M_{\rm dust}\, \kappa_{\rm dust}(\nu)} \times L_\nu^\star(\nu), \tag{10}$$

where $M_{\rm dust}$ is the total – non PAH – dust mass. This radiation density is constrained by the far-IR emission. Indeed, this part of the SED is not sensitive to the size distribution, since it is dominated by large grains at equilibrium with the radiation field, still small enough to be in the Rayleigh regime. Thus, we adopt the BARE-GR-S of the Zubko et al. (2004) model and fit the far-IR SED (usually the $IRAS_{60\mu m}$ and $IRAS_{100\mu m}$ bands) with:

$$L_\nu^{\text{FIR dust}}(\nu) = M_{\text{FIR dust}} \times \left(\zeta_{\rm gra} L_\nu^{\dagger\,\rm gra}(\nu) + \zeta_{\rm sil} L_\nu^{\dagger\,\rm sil}(\nu)\right), \tag{11}$$

where $L_\nu^{\dagger\,\rm gra(sil)}$ is the graphite (silicate) monochromatic luminosity per unit mass of dust. Since, the grains emitting in the far-IR are the largest, and they contain the essential of the mass, we assume that:

$$M_{\rm dust} \simeq M_{\text{FIR dust}}. \tag{12}$$

We will discuss, in §4, possible deviations to this relation.

Fig. 4 shows an example of a SED fitted in order to determine the radiation density. The B, V, H, K bands, at least, are required to constrain the burst parameters,

$M_{\rm young}, t_{\rm young}, M_{\rm old}, t_{\rm old}$. To constrain the parameters of the ISRF, Λ and $M_{\rm dust}$, we additionally need at least the 60 and 100 μm IRAS fluxes. The excess between $\sim$ 10 and $\sim$ 40 μm can be attributed either to an overabundance of small grains or to hotter regions, while a possible excess in the submillimeter could be attributed to colder shielded regions. We do not require energy conservation between the energy absorbed and reradiated by the dust, since we fit the SED only partially.

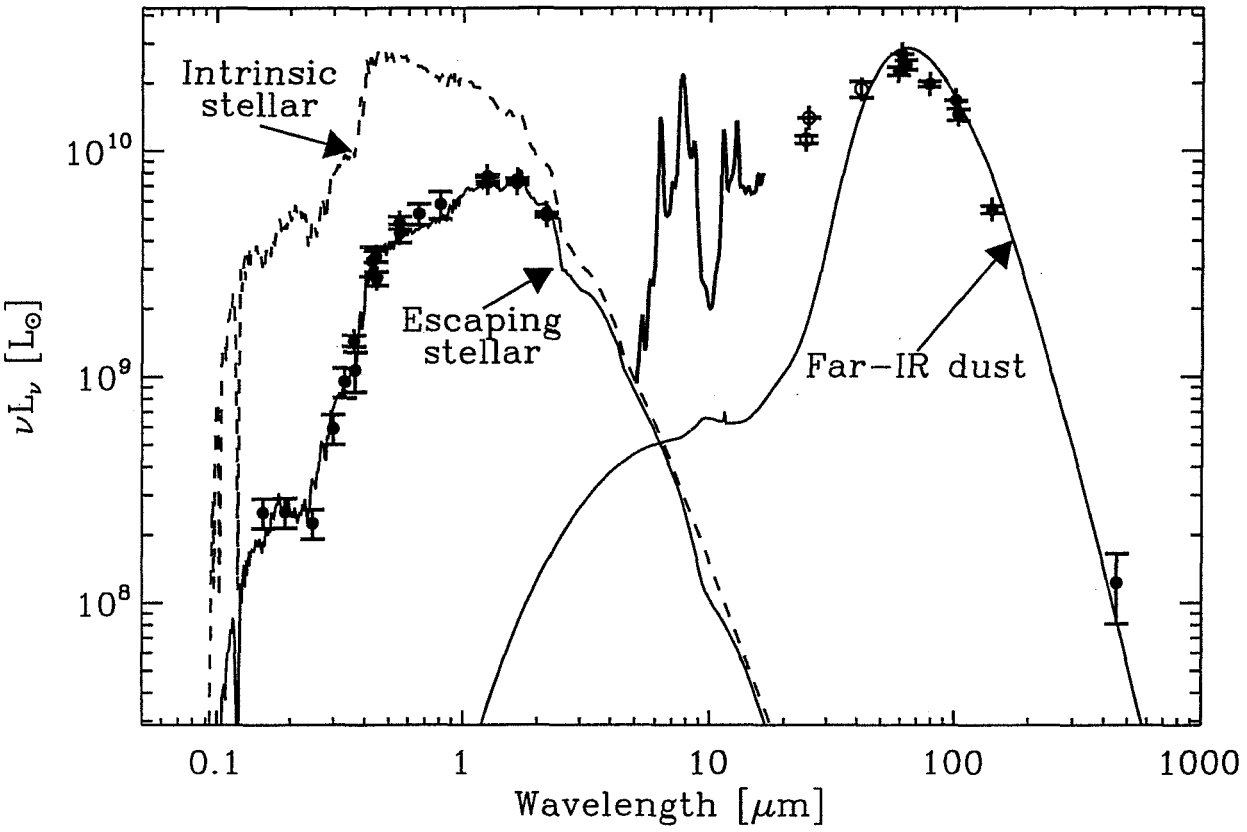

Fig. 4.— Determination of the intrinsic stellar radiation density. The symbols and the mid-IR spectrum are the observations. The mid-IR regime is purposely not fitted at this step. The open circles are the data which have not been used to constrain the ISRF.

3.3. Estimation of the PAH Mass

The radiation density in Eq. (10) is used to excite two components of neutral and ionised PAHs, with the BARE-GR-S size distribution of Zubko et al. (2004) and the Li &

Draine (2001) optical properties, taking into account the stochastic heating. The luminosity reemitted by the PAHs is:

$$L_\nu^{\rm PAH}(\nu) = M_{\rm PAH} \times \left([1 - f_+]\, L_\nu^{\dagger\,{\rm PAH}^0}(\nu) + f_+ L_\nu^{\dagger\,{\rm PAH}^+}(\nu) \right), \quad (13)$$

where $M_{\rm PAH}$ is the mass of PAHs, f_+, the mass fraction of cationic PAHs, and $L_\nu^{\dagger\,{\rm PAH}^0({\rm PAH}^+)}$, the luminosity per unit mass of PAHs. The free parameters controlling this component are f_+, and $M_{\rm PAH}$. We incorporate several other physical ingredients in order to fit the detailed observed mid-IR spectrum. A very hot grain (VHG) continuum is modeled with the sum of two modified black bodies, with the absorption efficiencies of graphite and silicate, $Q_{\rm abs}^i(a,\nu)$, and their densities ρ_i. This approximation can not be valid in the case of stochastically heated very small grains, however this analytical formulation is sufficient to subtract the underlying continuum present in all our spectra. A more sophisticated component would be underconstrained. The silicate feature in emission is usually not prominent, except in Mrk 153. The luminosity of this VHG continuum is:

$$L_\nu^{\rm VHG}(\nu) = \sum_i \frac{3\pi M_i^{\rm VHG}}{\rho_i} \left(\frac{Q_{\rm abs}^i(a_0,\nu)}{a_0} \right) \times B_\nu(\nu, T_i^{\rm VHG}), \quad (14)$$

for $i = \{graphite, silicate\}$. The masses $M_i^{\rm VHG}$, and the temperatures $T_i^{\rm VHG}$ are the only free parameters. The grain radius a_0 is arbitrarily fixed to 0.03 μm, the results being insensitive to its value.

The mid-IR contains several powerful emission lines. The brightests are usually the [Ar II]$_{6.98\mu m}$, [Ar III]$_{8.99\mu m}$, [S IV]$_{10.51\mu m}$, [Ne II]$_{12.81\mu m}$ and [Ne III]$_{15.56\mu m}$. We therefore add to the fit our mid-IR spectra $N_{\rm ion}$ ionic lines of luminosity $L_\nu^{\rm ion}$, with gaussian profiles:

$$L_\nu^{\rm ion}(\nu) = \sum_{i=1}^{\rm N_{ion}} L_i \frac{\sqrt{2}}{\sqrt{\pi}\Delta\nu} \times \exp\left[-2 \left(\frac{\nu - \nu_i}{\Delta\nu} \right)^2 \right]. \quad (15)$$

The width, $\Delta\nu$, is set by the spectral resolution. The only free parameters of this component are the various L_i. These lines are not used in this paper, we model them in order to properly subtract their contribution to the total spectrum.

Finally, all these components are attenuated by the escaping probability, $\mathcal{P}_{\rm esc}$. In some cases, where the sources are deeply embedded, the optical depth deduced from the UV can differ significantly from the one derived from the observed silicate feature absorption at 9.7 μm. This effect has been encountered in numerous *ISO* spectra (e.g. Thuan et al. 1999b; Gallais et al. 2004). Therefore, we determine another optical depth, $\tau^{\rm MIR}(\nu)$, from the fit of the mid-IR spectrum.

In conclusion, the spectrum is modeled by the following equation:

$$L_\nu^{\rm MIR}(\nu) = L_\nu^\star(\nu) \times \mathcal{P}_{\rm esc}(\tau,\omega) + \left(L_\nu^{\rm PAH}(\nu) + L_\nu^{\rm VHG}(\nu) + L_\nu^{\rm ion}(\nu)\right) \times \mathcal{P}_{\rm esc}(\tau^{\rm MIR},\omega), \qquad (16)$$

the stellar continuum being important only for elliptical galaxies. Fig. 5 demonstrates this method. From this fit, we derive the total PAH-to-total-gas mass ratio, $Z_{\rm PAH}$:

$$Z_{\rm PAH} = \frac{M_{\rm PAH}}{\mu\, M_{\rm H\,I}} \qquad \text{where} \qquad \mu = \frac{1}{1-Y-Z}, \qquad (17)$$

and Z is the metallicity of the galaxy. The mass fraction of carbon which is locked in PAHs is:

$$Z_{\rm C\ in\ PAHs} \simeq Z_{\rm PAH}. \qquad (18)$$

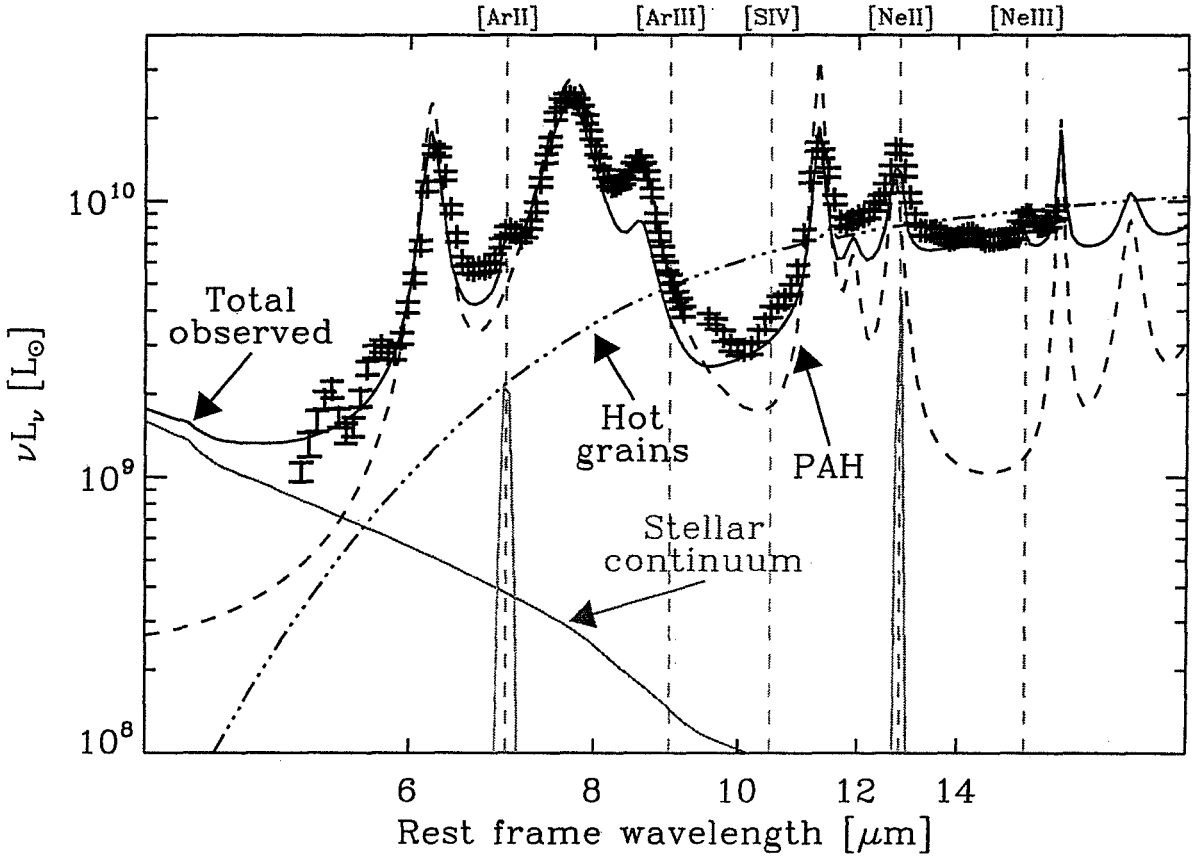

Fig. 5.— Determination of the PAH abundance. The error bars are the observed mid-IR spectrum. The dashed line is the sum of the PAH^0 and PAH^+ spectra. The dashed-dotted line is the intrinsic hot grain continuum. The black solid line is the attenuated sum of all these components, fitted to the observed spectrum.

4. THE PAH ABUNDANCE IN GALAXIES

4.1. Results of the SED Modeling

We applied the method described in §3.2 and 3.3, to the sample in Table 1. For each galaxy, we performed the SED and mid-IR spectrum fitting for the three dust compositions given in Table 2, and for the two geometries: uniform and thin shell. We show the figures obtained with Galactic extinction and uniform geometry, in Figs. 6 to 14. The other models give fits of the same quality, the main difference being due to the variations in the strength of the 9.7 μm silicate feature in extinction. The dispersion of the results given by the different models is an indication of their sensitivity to the model parameters. Consequently, the upper and lower limits presented in Fig. 15 and Table 3, are the maximum and minimum value of each quantity derived by the six models. In addition, these maximum and minimum values take into account the observational errors (e.g. the upper limit on the mass of PAHs is the value of the mass given by the model which gives the higher mass, when fitted through the higher end of the error bars on the observed spectrum). In most of the cases, the dispersion among the different models is larger than the observational error.

PAH features are not detected in I Zw 18, SBS 0335-052, Mrk 153, NGC 5253 and NGC 1399. For these galaxies, we get an upper limit by fitting the short-wavelength part of the mid-IR spectrum with the maximum PAH amount allowed by the observational errors.

I Zw 18: The H I extends far out of the star forming region. Instead of normalizing the dust masses by the value of $M_{\rm H\,I}$ in Table 1, we consider that the H I mass associated to the star forming region is the one of the object H I-A (van Zee et al. 1998), where $M_{\rm H\,I} = 4.4 \times 10^7\ M_\odot$.

SBS 0335-052: The 65 μm flux is the one reported by Hunt et al. (2005). The fit of this flux gives a far-IR dust temperature slightly colder than what we would obtain by fitting only the slope of the *Spitzer*/IRS spectrum. However, this gives a conservative solution, since we derive only an upper limit on the mass of PAHs, in this galaxy. The H I halo extends also far out of the star forming region. We assume that the star forming region has the same size than the optical galaxy, i.e. a radius of 1.6 kpc (6″). We derive the corresponding mass of H I, using the average column density of $N_{\rm H\,I} = 7.4 \times 10^{20}$ cm^{-2} reported by Pustilnik et al. (2001). We find $M_{\rm H\,I} = 4.6 \times 10^7\ M_\odot$.

VII Zw 403: This *Spitzer*/IRS spectrum of this galaxy has been studied by Wu et al. (2006). However, they did not report any PAH detection. The degradation of the spectral resolution that we performed on this spectra (see §2.3) increases the signal-to-noise ratio significantly. We report a 4σ detection of the 7.7 μm feature, and marginal

detections of the 6.2 and 8.6 μm features. This is the lowest metallicty PAH detection to date.

Haro 11: As quoted by Bergvall et al. (2000), the ratio $M_{\rm H\,I}/L_{\rm B} < 0.01$ is abnormally low in this galaxy. The low value of the H I mass explains the high value of its dust-to-gas mass ratio (Fig. 15). On the contrary, its PAH-to-far-IR-dust mass ratio is not peculiar. This source, at 92 Mpc, is one of the most distant object in our sample.

IC 342: This galaxy is located at 10° of Galactic latitude. Hence, it is highly extincted by the foreground, which explains the peculiar shape of its optical/near-IR observed SED.

Tol 89: The mid-IR spectrum of this galaxy samples only its nucleus. That is the reason why it underestimates the *Spitzer*/IRAC$_{8\mu m}$ flux. To be conservative, we derive the lower limit on the PAH mass by fitting the spectrum, and the upper limit, by fitting the broad band.

NGC 1399: This object is a cD galaxy. Its interstellar medium is likely very tenuous and the mid-IR emission is dominated by the contribution of evolved stars. It has not been represented on the upper panel of Fig. 15, since we only know the upper limits on the PAH and H I gas masses. However, it is shown on the lower panel; the higher open circle is the ratio between the upper limit on the PAH mass and the lower limit on the dust mass.

Circinus: This galaxy is located at Galactic latitude below 5°. Like IC 342, its optical fluxes are very uncertain.

NGC 6240 and Arp 220: These two objects are the (U)LIRGs of our sample. In particular, the PAH-to-neutral-gas mass ratio of the most luminous, Arp 220, is very low.

The top panel of Fig. 15 shows the variation of the PAH and FIR-dust to gas mass ratios with the metallicity of the interstellar medium. Each individual galaxy can be seen as a snapshot of galaxy evolution, at a given time. First, we note that the Galactic values of the dust-to-gas mass ratios are in agreement with the one of the other galaxies, around the same metallicity. These Galactic values were derived by Zubko et al. (2004), from the fit of the emission and extinction of the diffuse interstellar medium, with further constraints from the elemental depletion pattern. Thus, it is a very reliable estimation. This comparison confirms that our method does not overlook a significant amount of dust, at least around the solar metallicity. Second, the trends of $Z_{\rm PAH}$ and $Z_{\rm FIR\text{-}dust}$, with the metallicity are not identical. Our sample spreads two orders of magnitude in metallicity. We can see that the PAH-to-gas mass ratio rises by five orders of magnitudes, while the FIR-dust-to-gas mass

ratio, by only three. This differential evolution is illustrated in the lower panel of Fig. 15, showing the PAH-to-FIR-dust mass ratio. This figure is the analog of Fig. 1, but instead of considering integrated fluxes, it deals with abundances. The PAH-to-FIR-dust mass ratio rises by two orders of magnitude, over our sample, while the $\mathrm{IRAC}_{8\mu m}/\mathrm{MIPS}_{24\mu m}$ band ratio varies only by one order of magnitude.

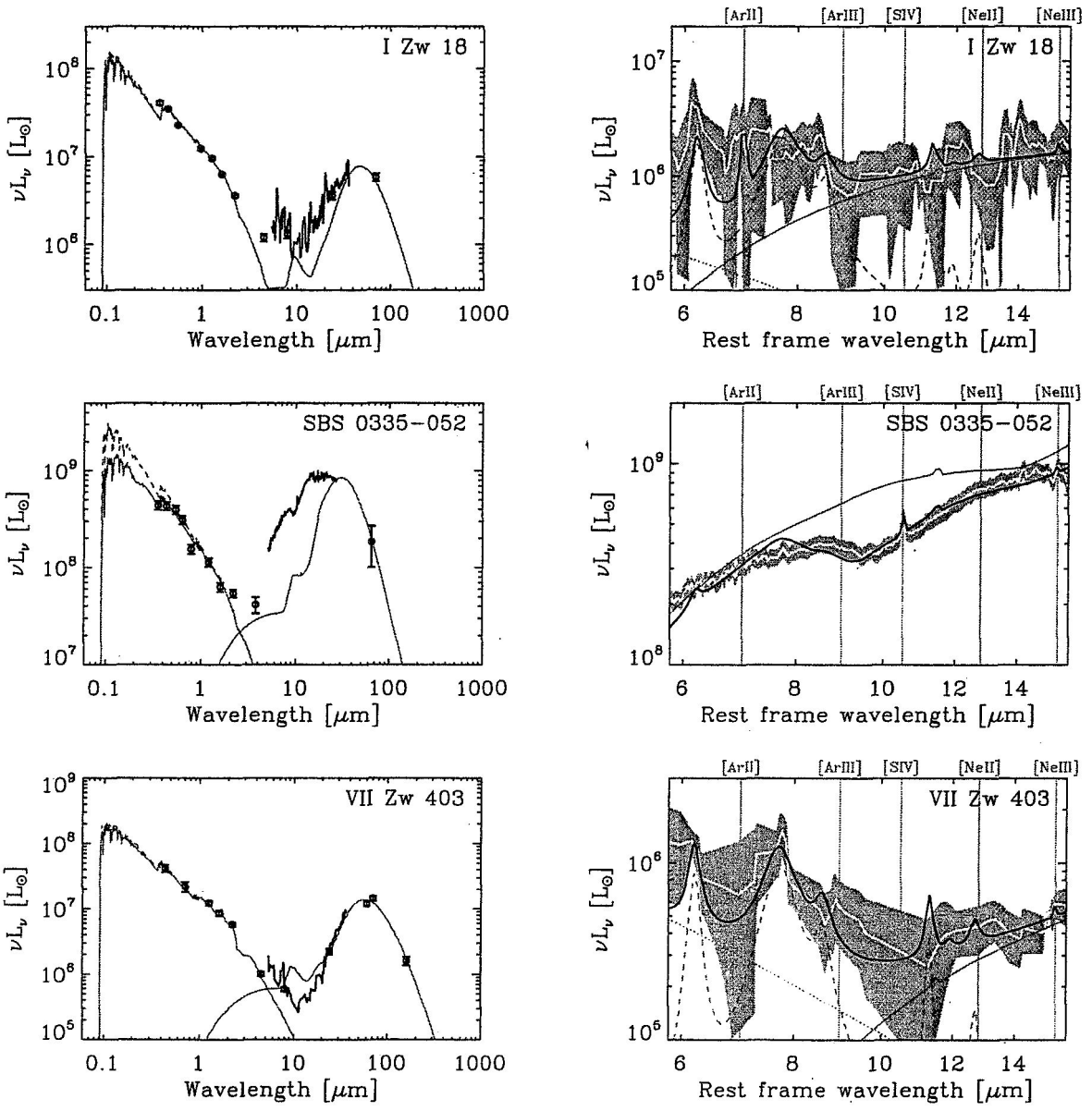

Fig. 6.— Fit of the galaxies' SEDs. These figures are the analogs of Figs. 4 and 5, for all the galaxies. We show only the model for a Galactic extinction law and a uniform sphere geometry. The *left panel* shows the fit of the total SED. The normal lines are the components of the model, the escaping stellar and dust emission being plotted with solid lines, and the intrinsic stellar with dashed lines. The circles with error bars are the broad-band observations, and the thick line is the observed mid-IR spectrum. The *right panel* shows the detailed fit of the mid-IR spectrum. The grey region is the observed spectrum (white line) $\pm 1\sigma$, the grey dotted line is the stellar continuum, the grey dashed line, the sum of cationic and neutral PAH emission, the grey solid line, the very hot grain continuum, and the thick line, the attenuated sum of all the components. For clarity, we did not represent the ionic lines, although they are part of the final fit.

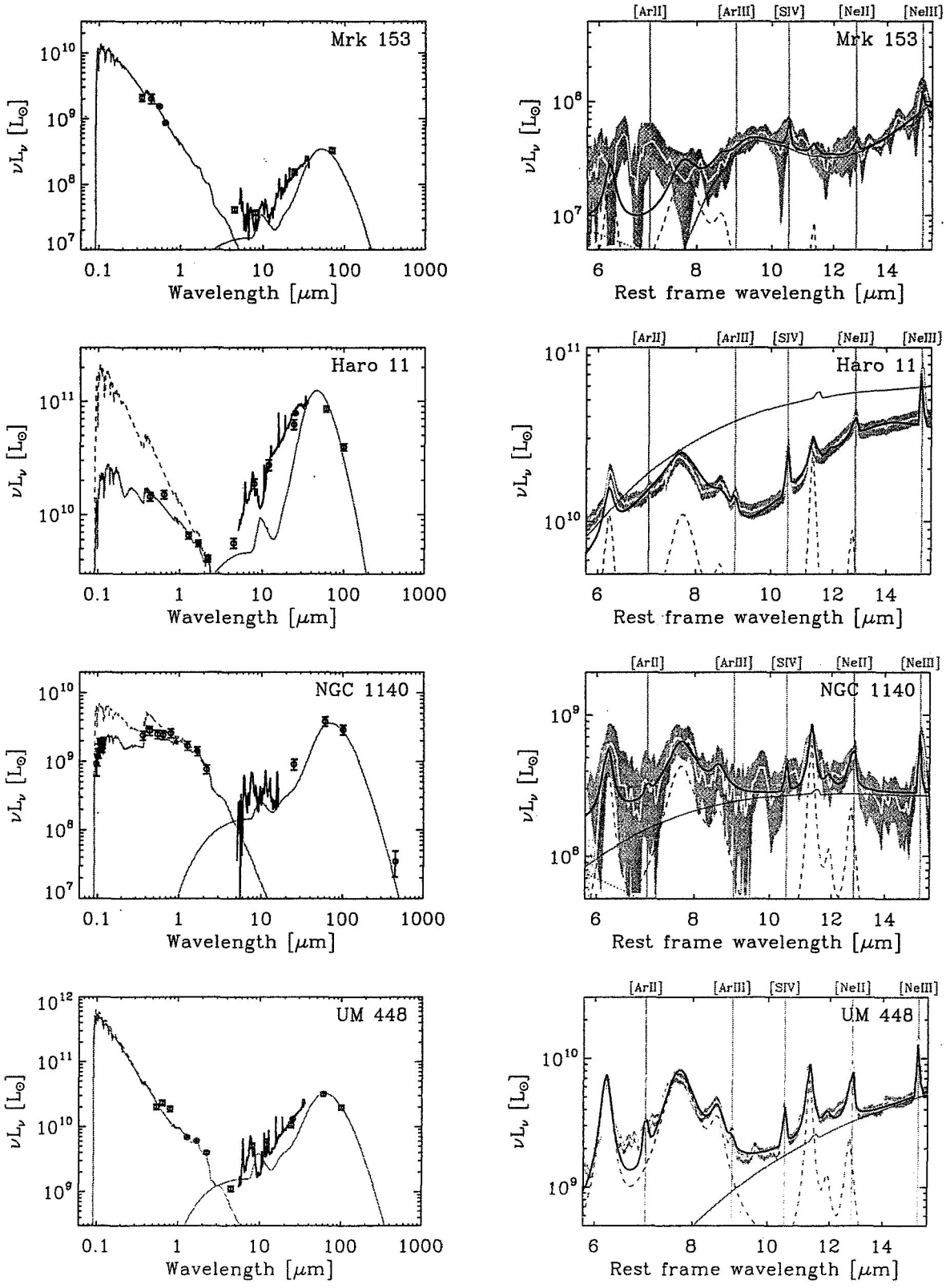

Fig. 7.— Fit of the galaxies' SEDs. See Fig. 6 for details.

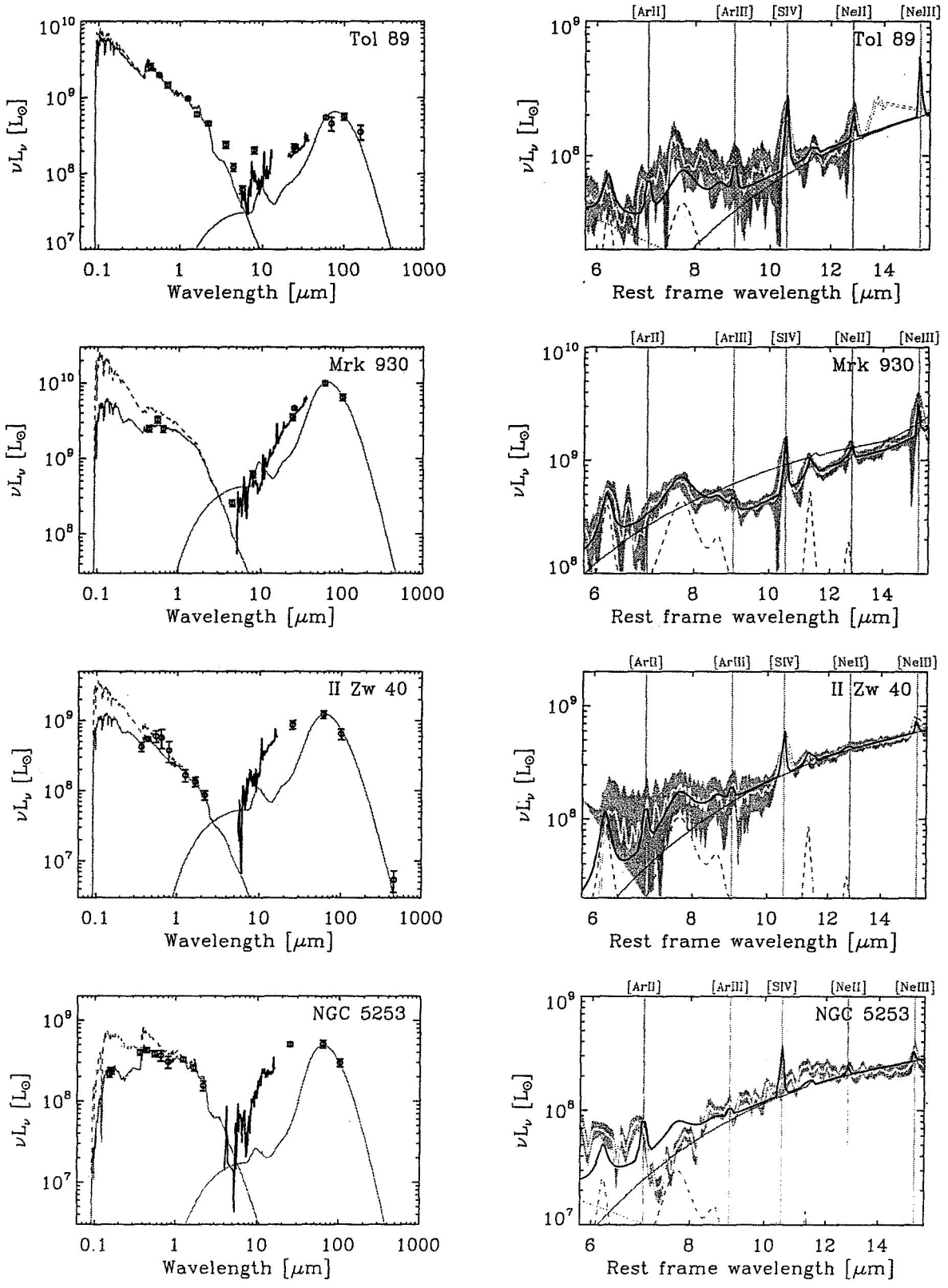

Fig. 8.— Fit of the galaxies' SEDs. See Fig. 6 for details.

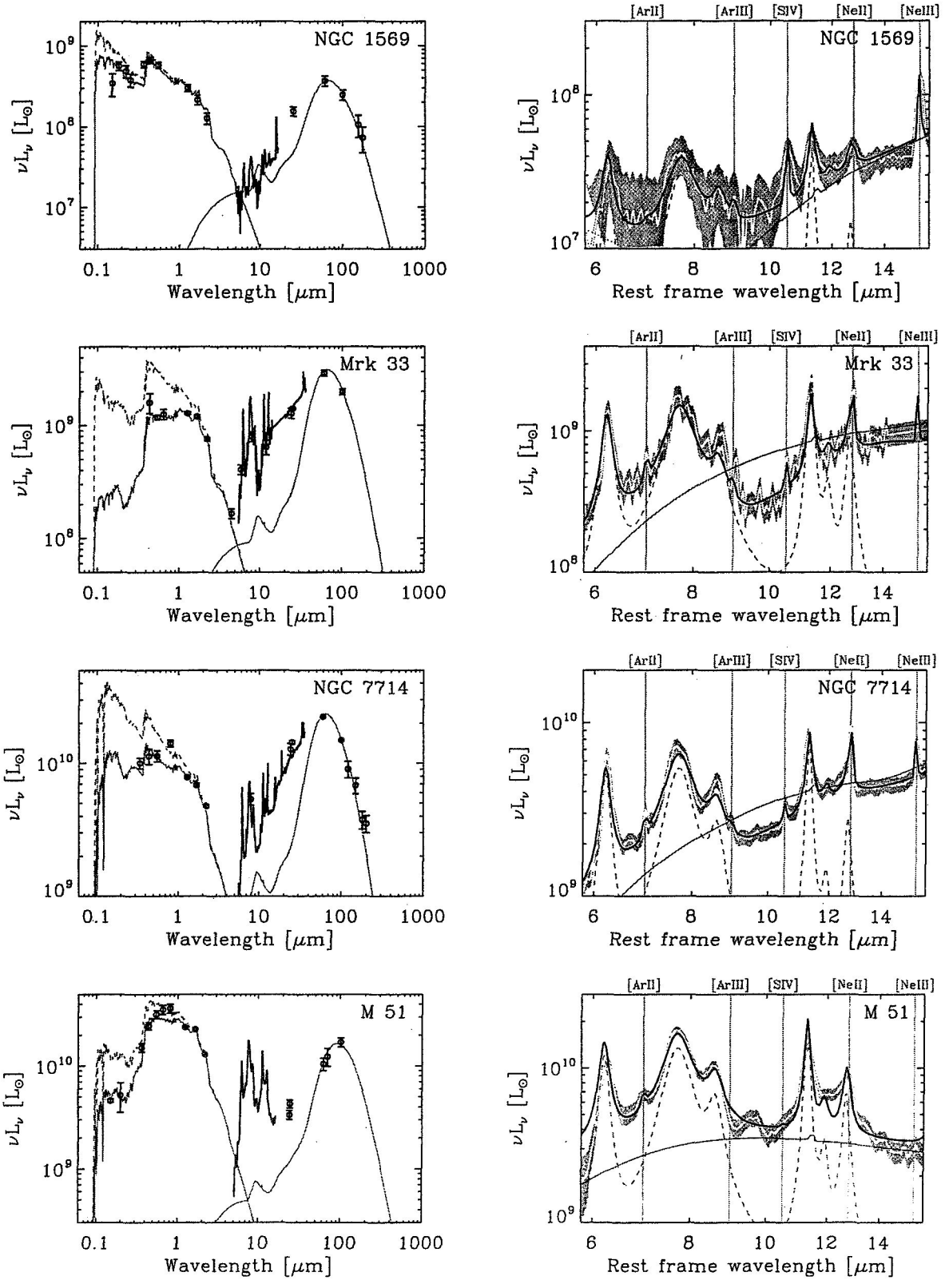

Fig. 9.— Fit of the galaxies' SEDs. See Fig. 6 for details.

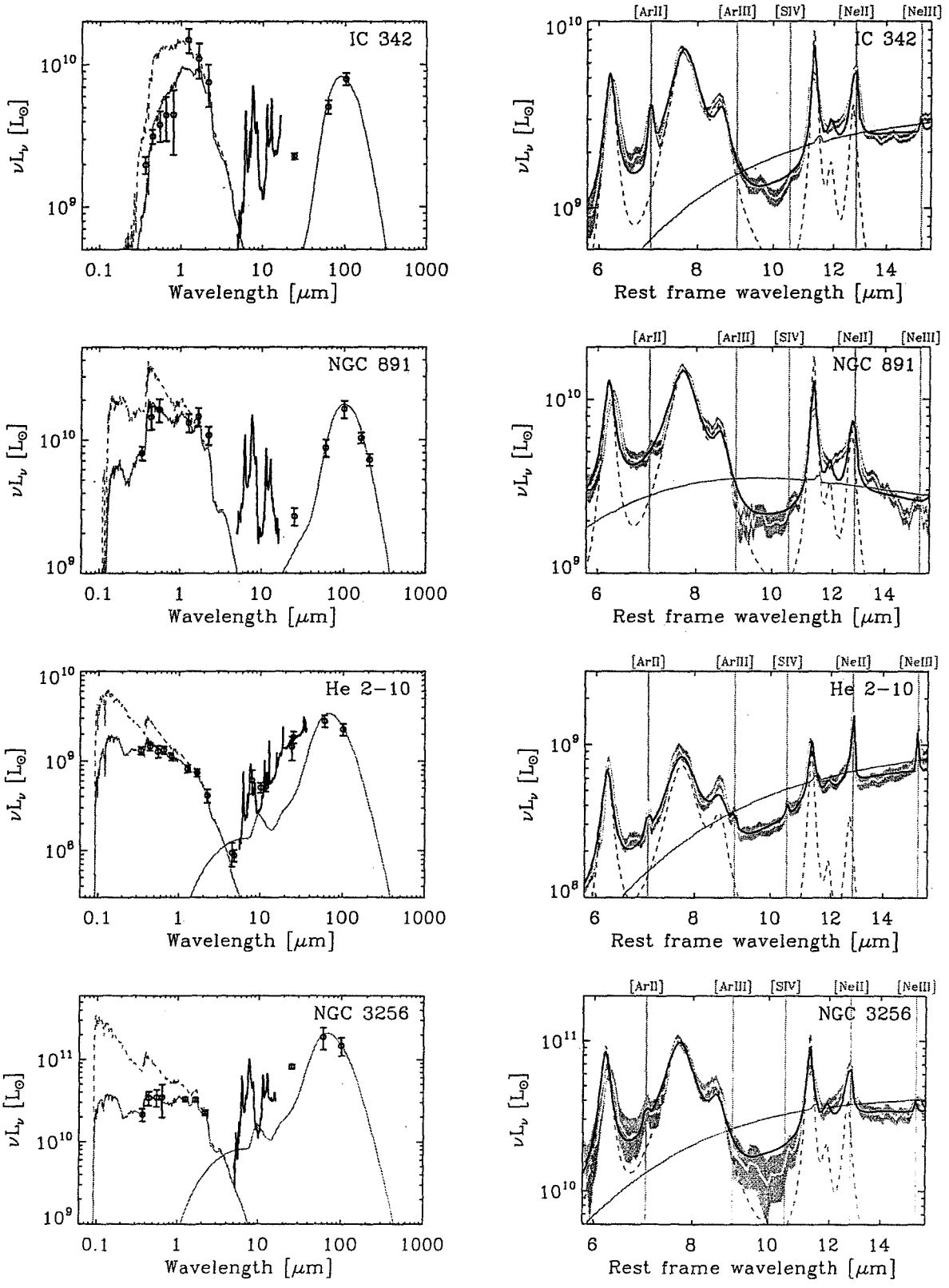

Fig. 10.— Fit of the galaxies' SEDs. See Fig. 6 for details.

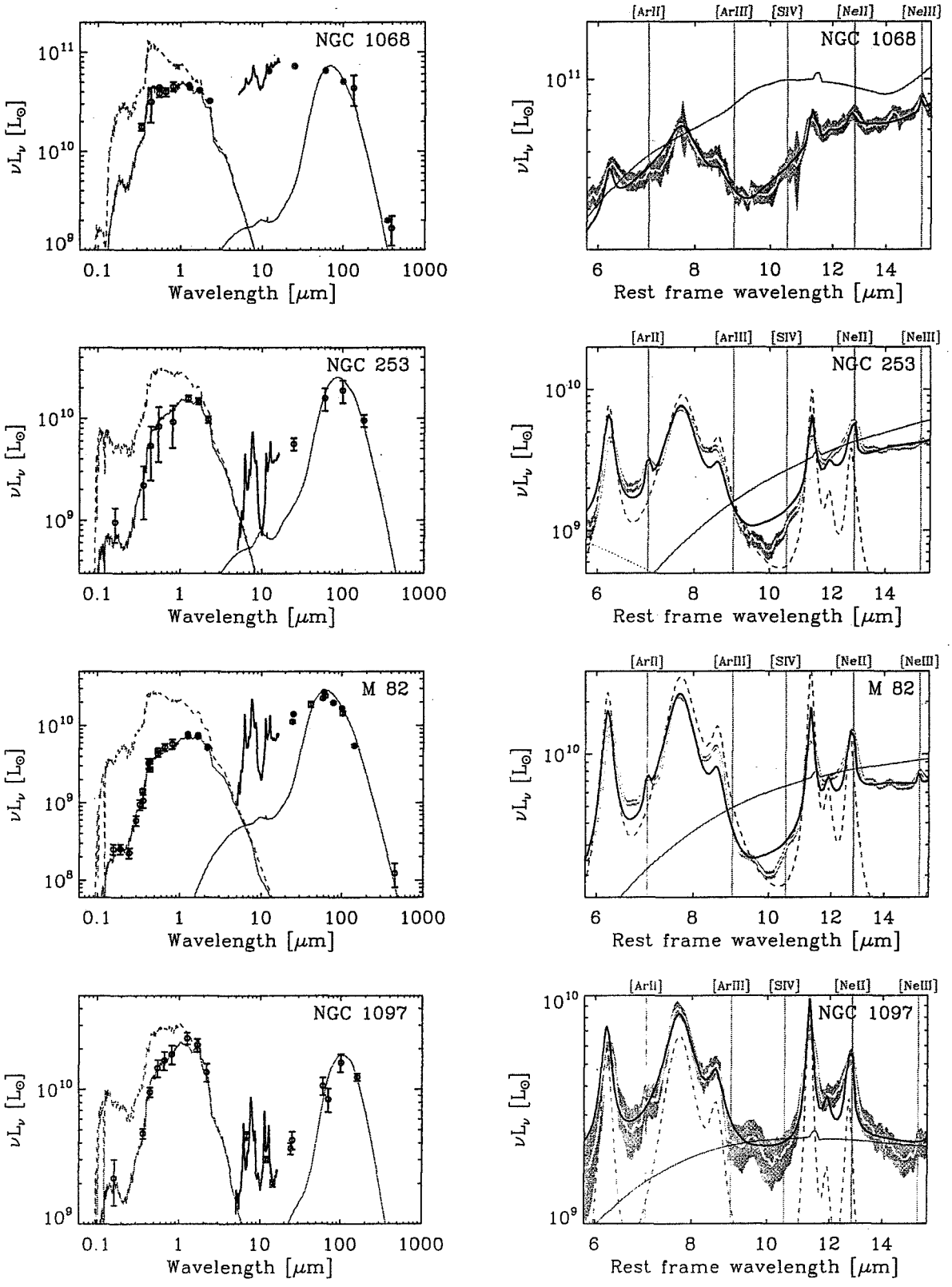

Fig. 11.— Fit of the galaxies' SEDs. See Fig. 6 for details.

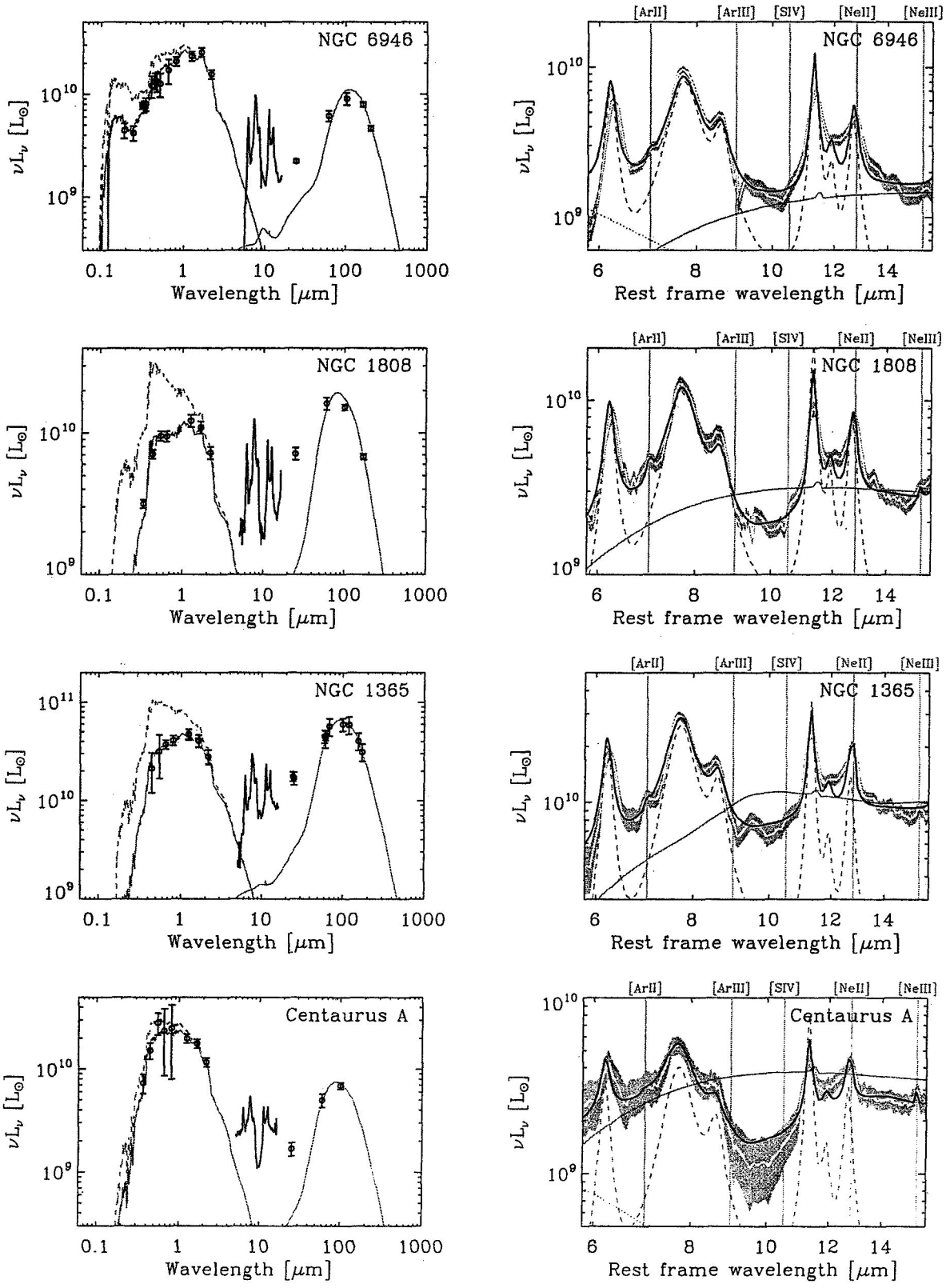

Fig. 12.— Fit of the galaxies' SEDs. See Fig. 6 for details.

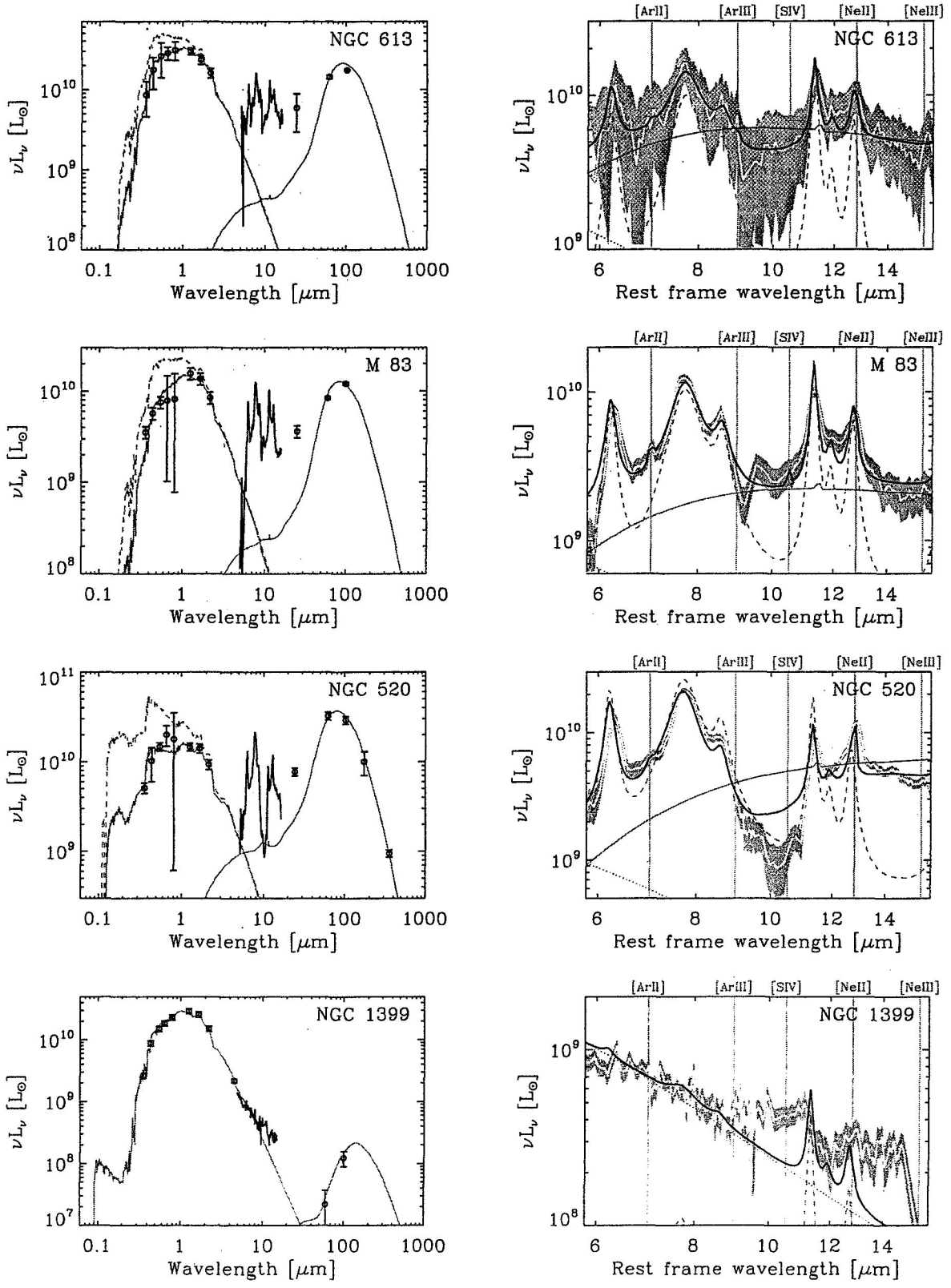

Fig. 13.— Fit of the galaxies' SEDs. See Fig. 6 for details.

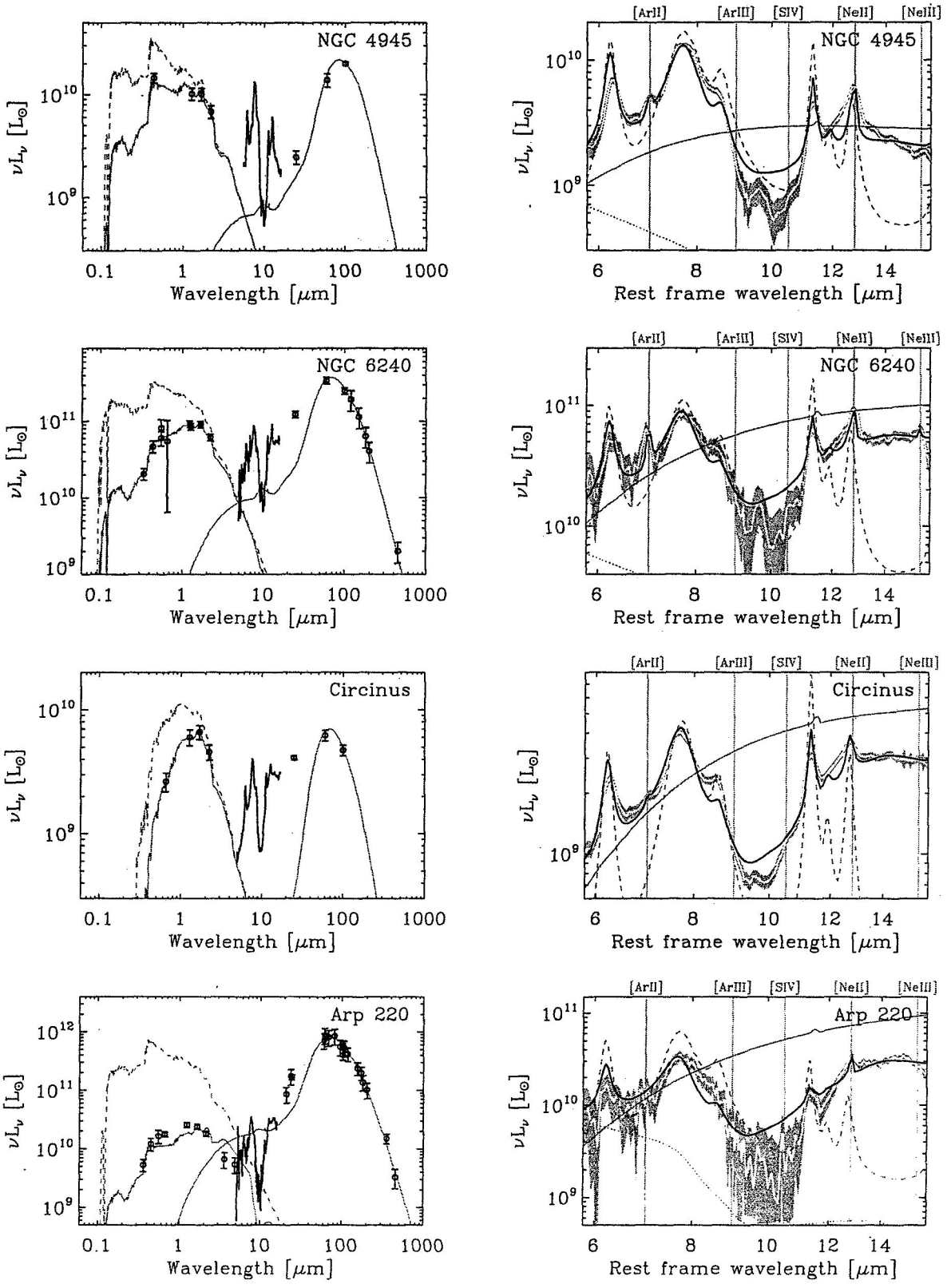

Fig. 14.— Fit of the galaxies' SEDs. See Fig. 6 for details.

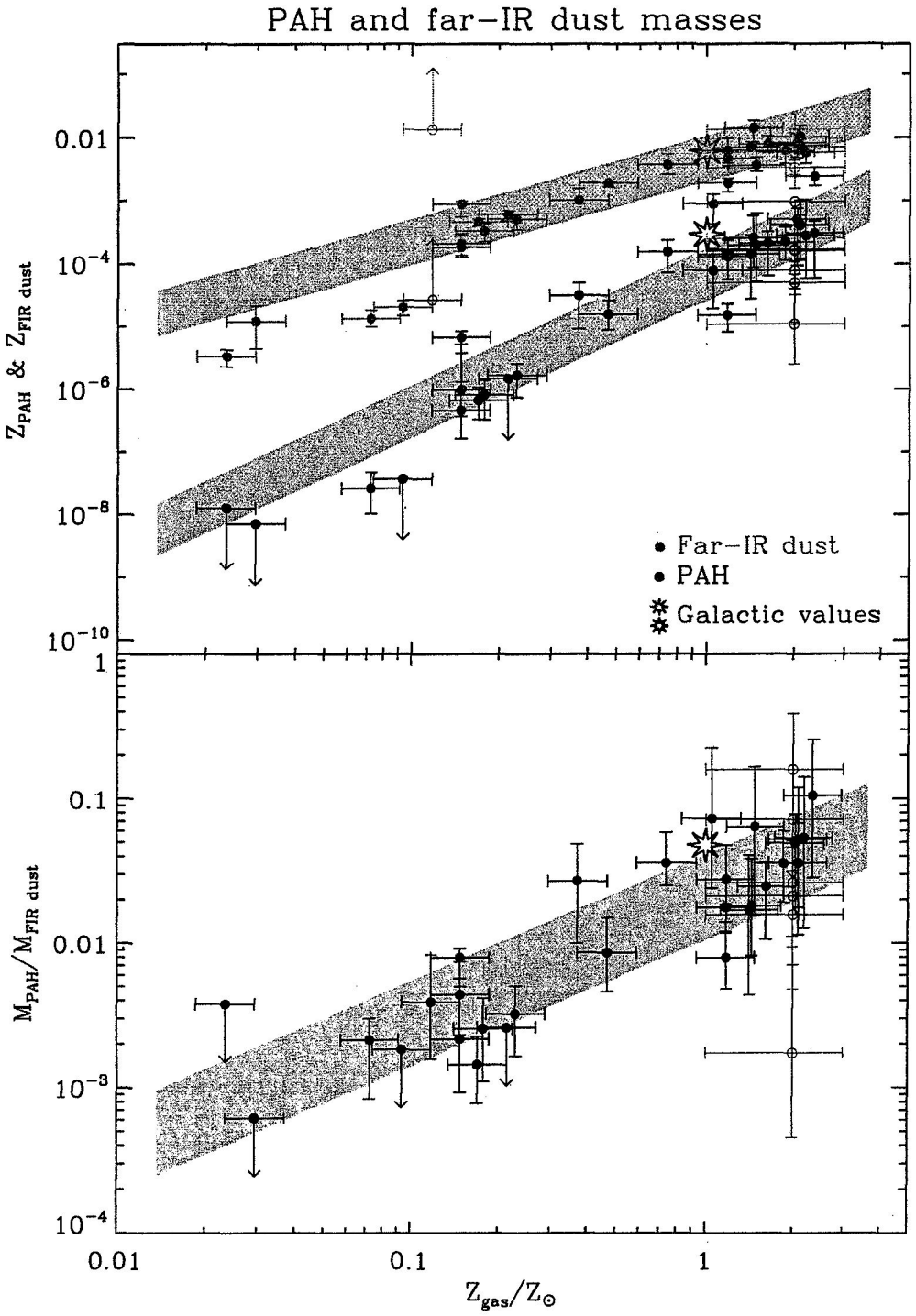

Fig. 15.— Top panel: dust-to-gas mass ratio for PAHs, $Z_{\rm PAH}$, and the dust that gives rise to the far-IR emission, $Z_{\rm FIR\ dust}$, as a function of metallicity. Bottom panel: mass ratio of PAH-to-far-IR-dust, as a function of metallicity. The circles correspond to galaxies and the open stars to the the diffuse Galactic ISM (Zubko et al. 2004). The filled circles are the reliable measurements, and the open circles are the ones which are considered uncertain. The grey stripes are the $\pm 1\sigma$ linear correlation, in logarithmic scale. These figures show the two distinct evolutionary trends of $Z_{\rm PAH}$ and $Z_{\rm FIR\text{-}dust}$ with metallicity.

Table 3. SED modeling results.

Name	Z ($Z_\odot$)	$M_{\rm PAH}$ ($M_\odot$)	f_+	$M_{\rm dust}$ ($M_\odot$)	$L^{\rm dust}$ ($10^8\ L_\odot$)	$L^\star$ ($10^8\ L_\odot$)	Λ ($\rm g\,cm^{-2}$)	$\Lambda_{\rm MIR}$ ($\rm g\,cm^{-2}$)
18	$0.023^{+0.006}_{-0.005}$	$\lesssim 1.3$	...	200 ± 60	$0.11^{+0.01}_{-0.01}$	$1.38^{+0.04}_{-0.05}$	$(1.9 \pm 1.2) \times 10^{-6(?)}$	$1.9^{+2.6}_{-1.9} \times 10^{-4(?)}$
0335-052	$0.030^{+0.008}_{-0.006}$	$\lesssim 0.5$	...	740^{+580}_{-470}	$13.6^{+6.2}_{-6.2}$	$26.6^{+5.8}_{-6.7}$	$1.4^{+2.7}_{-1.2} \times 10^{-5}$	$3.6^{+2.8}_{-1.6} \times 10^{-4}$
Tw 403	$0.072^{+0.019}_{-0.015}$	$2.4^{+1.9}_{-2.5}$	...	$1.2^{+0.5}_{-0.3} \times 10^3$	$0.16^{+0.02}_{-0.02}$	$3.2^{+0.9}_{-1.6}$	$1.2^{+0.5}_{-0.3} \times 10^{-6}$	$1.1^{+0.5}_{-1.1} \times 10^{-6}$
153	$0.093^{+0.024}_{-0.019}$	$\lesssim 60$	...	$(1.8 \pm 0.5) \times 10^4$	4.5 ± 0.5	120 ± 4030	$9.5^{+2.7}_{-5.7} \times 10^{-7}$	$\lesssim 2 \times 10^{-6}$
11	$0.12^{+0.03}_{-0.02}$	$8.7^{+8.1}_{-5.2} \times 10^3$	25^{+62}_{-15}%	$2.2^{+0.3}_{-0.4} \times 10^6$	$(1.7 \pm 0.1) \times 10^3$	$1.8^{+0.2}_{-0.3} \times 10^3$	$0.8^{+1.5}_{-0.6} \times 10^{-4}$	$7.8^{+6.9}_{-4.4} \times 10^{-4}$
1140	$0.15^{+0.04}_{-0.03}$	$6.8^{+2.3}_{-4.3} \times 10^3$	41^{+2}_{-2}%	$1.3^{+0.7}_{-0.4} \times 10^6$	53^{+12}_{-10}	110 ± 20	$2.8^{+2.7}_{-1.9} \times 10^{-5}$	$3.5^{+3.4}_{-2.1} \times 10^{-5}$
148	$0.15^{+0.04}_{-0.03}$	$4.2^{+1.1}_{-1.9} \times 10^4$	62^{+3}_{-19}%	$5.6^{+0.6}_{-2.1} \times 10^6$	490 ± 40	$3.9^{+0.6}_{-1.0} \times 10^3$	$2.7^{+1.8}_{-1.5} \times 10^{-6}$	$2.9^{+2.1}_{-2.8} \times 10^{-4}$
9	$0.15^{+0.04}_{-0.03}$	$0.8^{+8.3}_{-0.5} \times 10^3$	...	$3.7^{+1.6}_{-1.3} \times 10^5$	$10.0^{+0.3}_{-0.2}$	88^{+27}_{-20}	$3.4^{+4.0}_{-2.4} \times 10^{-6}$	$\lesssim 1.6 \times 10^{-4}$
930	0.17 ± 0.04	$2.5^{+1.5}_{-1.3} \times 10^3$	50^{+1}_{-5}%	$1.7^{+0.2}_{-0.3} \times 10^6$	140 ± 10	240^{+50}_{-60}	$3.8^{+3.1}_{-3.0} \times 10^{-5}$	$3.6^{+2.7}_{-1.8} \times 10^{-4}$
40	$0.18^{+0.05}_{-0.04}$	$4.6^{+3.2}_{-2.7} \times 10^2$	99^{+1}_{-31}%	$(1.9 \pm 0.6) \times 10^5$	23 ± 3	30^{+4}_{-3}	$2.3^{+2.9}_{-1.5} \times 10^{-5}$	$\lesssim 2.0 \times 10^{-5}$
5253	$0.21^{+0.06}_{-0.05}$	$\lesssim 200$	...	$7.4^{+1.2}_{-1.6} \times 10^4$	$10.8^{+1.2}_{-1.2}$	16^{+3}_{-2}	$3.3^{+3.7}_{-2.2} \times 10^{-5}$	$\lesssim 3.5 \times 10^{-6}$
1569	$0.23^{+0.06}_{-0.05}$	$(2.9 \pm 1.6) \times 10^2$	39^{+1}_{-8}%	$8.9^{+1.9}_{-2.9} \times 10^4$	5.5 ± 0.9	$19.2^{+1.9}_{-2.1}$	$1.1^{+1.3}_{-0.7} \times 10^{-5}$	$\lesssim 1.9 \times 10^{-5}$
33	$0.37^{+0.10}_{-0.08}$	$1.8^{+1.1}_{-1.3} \times 10^4$	38^{+30}_{-3}%	$5.9^{+3.1}_{-0.6} \times 10^5$	$53.1^{+4.6}_{-3.9}$	62 ± 14	$9.0^{+38}_{-6.8} \times 10^{-4}$	$\lesssim 8.9 \times 10^{-4}$
7714	$0.47^{+0.12}_{-0.10}$	$3.6^{+2.4}_{-1.6} \times 10^4$	39^{+2}_{-1}%	$4.4^{+0.1}_{-0.6} \times 10^6$	412^{+9}_{-2}	600^{+140}_{-100}	$3.8^{+2.6}_{-2.8} \times 10^{-5}$	$2.6^{+1.5}_{-1.1} \times 10^{-4}$
	$0.74^{+0.19}_{-0.15}$	$(1.1 \pm 0.6) \times 10^6$	44 ± 1%	$2.5^{+1.1}_{-0.8} \times 10^7$	300^{+70}_{-60}	780 ± 80	$2.9^{+4.5}_{-2.0} \times 10^{-5}$	$4.1^{+3.2}_{-1.2} \times 10^{-5}$
2	$1.0^{+0.3}_{-0.2}$	$1.4^{+1.7}_{-1.1} \times 10^6$	56^{+2}_{-6}%	$1.6^{+0.7}_{-0.8} \times 10^7$	150 ± 20	240^{+40}_{-50}	$9.2^{+38.1}_{-7.4} \times 10^{-5}$	$2.9^{+2.6}_{-0.8} \times 10^{-4}$
891	$1.2^{+0.3}_{-0.2}$	$1.5^{+1.0}_{-0.9} \times 10^6$	52^{+1}_{-3}%	$4.9^{+1.3}_{-1.2} \times 10^7$	290^{+50}_{-40}	580 ± 130	$4.4^{+14.8}_{-3.3} \times 10^{-5}$	$4.2^{+2.8}_{-1.6} \times 10^{-4}$
10	$1.2^{+0.3}_{-0.2}$	$6.5^{+3.2}_{-3.0} \times 10^3$	46^{+1}_{-7}%	$8.1^{+1.4}_{-2.3} \times 10^5$	$53.6^{+9.2}_{-9.3}$	75^{+14}_{-12}	$3.6^{+10.4}_{-2.7} \times 10^{-5}$	$2.9^{+2.1}_{-1.2} \times 10^{-4}$
3256	$1.2^{+0.3}_{-0.2}$	$1.1^{+0.2}_{-0.6} \times 10^6$	53^{+3}_{-2}%	$5.3^{+2.8}_{-1.9} \times 10^7$	$3.2 \pm 1.0 \times 10^3$	$3.3^{+1.0}_{-0.8} \times 10^3$	$8.9^{+40.1}_{-7.3} \times 10^{-5}$	$4.1^{+2.5}_{-1.7} \times 10^{-4}$
1068	$1.4^{+0.4}_{-0.3}$	$4.4^{+4.4}_{-3.6} \times 10^5$	48^{+1}_{-5}%	$2.2^{+0.5}_{-0.2} \times 10^7$	$2.1^{+0.1}_{-0.2} \times 10^3$	$1.8 \pm 0.7 \times 10^3$	$8.4^{+29.7}_{-6.0} \times 10^{-5}$	$3.7^{+3.5}_{-1.8} \times 10^{-4}$
253	$1.4^{+0.4}_{-0.3}$	$6.4^{+7.9}_{-4.2} \times 10^5$	59^{+4}_{-6}%	$3.5^{+1.1}_{-1.4} \times 10^7$	370 ± 100	540^{+310}_{-300}	$1.3^{+4.2}_{-1.0} \times 10^{-4}$	$6.1^{+4.2}_{-1.9} \times 10^{-4}$
	$1.5^{+0.4}_{-0.3}$	$2.4^{+5.4}_{-1.8} \times 10^5$	57^{+2}_{-6}%	$4.5^{+1.6}_{-0.9} \times 10^6$	450^{+20}_{-30}	440 ± 30	$2.8^{+11.5}_{-2.4} \times 10^{-4}$	$6.1^{+5.2}_{-2.4} \times 10^{-4}$
1097	$1.6^{+0.4}_{-0.3}$	$1.5^{+0.8}_{-1.1} \times 10^6$	43^{+2}_{-3}%	$5.6^{+1.9}_{-1.5} \times 10^7$	290 ± 60	590^{+80}_{-70}	$6.1^{+21.3}_{-4.7} \times 10^{-5}$	$1.7^{+1.0}_{-0.7} \times 10^{-4}$
6946	$1.9^{+0.5}_{-0.4}$	$1.7^{+1.2}_{-0.9} \times 10^6$	36^{+1}_{-2}%	$4.8^{+1.0}_{-1.8} \times 10^7$	190^{+30}_{-20}	600 ± 120	$2.6^{+6.7}_{-1.6} \times 10^{-5}$	$1.8^{+0.9}_{-0.7} \times 10^{-4}$
1808	$2.0^{+0.5}_{-0.4}$	$1.3^{+0.7}_{-1.0} \times 10^6$	33^{+2}_{-1}%	$2.1^{+1.3}_{-0.9} \times 10^7$	340 ± 110	420^{+120}_{-100}	$1.1^{+2.6}_{-0.9} \times 10^{-4}$	$2.8^{+3.2}_{-1.7} \times 10^{-4}$
520	$\simeq 2 \pm 1^{(?)}$	$7.9^{+6.8}_{-5.6} \times 10^5$	81^{+1}_{-4}%	$2.8^{+0.5}_{-0.7} \times 10^7$	560^{+70}_{-60}	760^{+320}_{-330}	$1.5^{+3.0}_{-0.9} \times 10^{-4}$	$6.4^{+4.4}_{-2.7} \times 10^{-4}$
1399	$\simeq 2 \pm 1^{(?)}$	$\lesssim 1.0 \times 10^{6(?)}$	...	$\gtrsim 4.5 \times 10^{5(?)}$	$\gtrsim 1.50 \times 10^{3(?)}$	420^{+40}_{-50}	$1.0^{+4.5}_{-0.9} \times 10^{-6(?)}$	$\lesssim 1.0 \times 10^{-6(?)}$
4945	$\simeq 2 \pm 1^{(?)}$	$4.8^{+5.6}_{-2.8} \times 10^5$	73 ± 1%	$2.0^{+0.7}_{-0.5} \times 10^7$	300 ± 50	530^{+90}_{-70}	$7.2^{+6.3}_{-5.2} \times 10^{-5}$	$7.2^{+6.0}_{-3.1} \times 10^{-4}$
us	$\simeq 2 \pm 1^{(?)}$	$3.8^{+4.4}_{-2.9} \times 10^5$	43 ± 1%	$1.9^{+0.8}_{-0.4} \times 10^6$	130^{+10}_{-20}	160 ± 30	$1.5^{+6.4}_{-1.0} \times 10^{-4}$	$8.7^{+8.9}_{-4.1} \times 10^{-4}$
3240	$\simeq 2 \pm 1^{(?)}$	$2.1^{+1.5}_{-1.6} \times 10^6$	40^{+2}_{-11}%	$1.2 \pm 0.3 \times 10^8$	$5.4^{+0.6}_{-0.8} \times 10^3$	$5.8^{+1.2}_{-1.6} \times 10^3$	$2.1^{+8.3}_{-1.8} \times 10^{-4}$	$9.3^{+10.1}_{-4.0} \times 10^{-4}$
20	$\simeq 2 \pm 1^{(?)}$	$4.3^{+22.4}_{-3.3} \times 10^5$	97^{+3}_{-29}%	$2.7^{+1.6}_{-1.0} \times 10^8$	$1.0 \pm 0.3 \times 10^4$	$1.0^{+0.4}_{-0.3} \times 10^4$	$2.4^{+11.4}_{-2.3} \times 10^{-3}$	$1.7^{+3.4}_{-1.1} \times 10^{-3}$
1365	$2.1^{+0.5}_{-0.4}$	$7.4^{+3.4}_{-5.2} \times 10^6$	53^{+1}_{-30}%	$1.9^{+0.9}_{-0.8} \times 10^8$	$1.1 \pm 0.2 \times 10^3$	$1.6 \pm 0.7 \times 10^3$	$1.2^{+5.0}_{-0.9} \times 10^{-4}$	$3.0^{+7.6}_{-1.6} \times 10^{-4}$
arus A	$2.1^{+0.5}_{-0.4}$	$6.5^{+9.2}_{-4.7} \times 10^5$	30^{+1}_{-2}%	$1.1^{+0.3}_{-0.2} \times 10^7$	137 ± 21	480 ± 90	$2.7^{+11.0}_{-1.9} \times 10^{-5}$	$5.8^{+5.3}_{-2.5} \times 10^{-4}$
513	$2.2^{+0.6}_{-0.5}$	$1.5^{+3.9}_{-1.2} \times 10^6$	38 ± 1%	$3.0^{+0.8}_{-1.0} \times 10^7$	360^{+40}_{-30}	740^{+410}_{-340}	$5.7^{+12.7}_{-3.8} \times 10^{-5}$	$2.7^{+2.3}_{-1.5} \times 10^{-4}$

4.2. A Model for the Gas and Dust Evolution

We have developed a one-zone single-phase chemical evolution model, to follow the abundances and composition of the dust and the metallicty as a function of time, in order to interpret the results of our SED modeling. In this section, we will give a brief description of the physical processes which are incorporated. A more detailed discussion can be found in Dwek (1998) and Dwek et al. (2007). Assuming a common star formation history, we will use this model to interpret the observed evolutionary trend of galaxies' SED with metallicity, **on a global scale.**

4.2.1. Metal Enrichment and Gas Evolution

In the present paper, we consider a closed box model. We consider the delayed injection of material by different stellar progenitors, but we assume that the mixing of the elements in the ISM is instantaneous. We adopt a Salpeter initial mass function IMF, $\phi(m)$, defined as follows:

$$\begin{aligned} \phi(m) \propto m^{-2.35} \qquad & \text{for} \qquad m_l < m < m_u \\ & \text{normalised to} \quad \int_{m_l}^{m_u} \phi(m)\, \mathrm{d}m = 1 \\ & \text{with} \quad \begin{cases} m_l &= 0.1\ M_\odot \\ m_u &= 100\ M_\odot \end{cases} \end{aligned} \tag{19}$$

where m is the mass of individual stars. We define the average stellar mass:

$$\langle m \rangle \equiv \int_{m_l}^{m_u} m\, \phi(m)\, \mathrm{d}m. \tag{20}$$

The evolution of the gas mass surface density, $\Sigma_{\rm gas}(t)$, with the time t, is:

$$\frac{\mathrm{d}\Sigma_{\rm gas}(t)}{\mathrm{d}t} = -\Sigma_{\rm SFR}(t) + \int_{m_l}^{m_u} \Sigma_{\rm SFR}(t - \tau(m))\, \frac{m_{\rm ej}(m)}{\langle m \rangle}\, \phi(m)\, \mathrm{d}m, \tag{21}$$

where $\Sigma_{\rm SFR}(t)$ is the mass of star formed per unit time and per unit surface area, $\tau(m)$, the lifetime of a star of mass m, and $m_{\rm ej}(m)$, its mass of gas returned to the ISM. The first term of the right hand side of Eq. (21) is the amount of gas removed by the star formation, and the second term, is the delayed injection of the gas (H, He and metals), by the various progenitors. The ISM metallicity, is defined as:

$$Z_{\rm ISM}(t) \equiv Z_{\rm gas}(t) + Z_{\rm dust}(t), \tag{22}$$

Table 3—Continued

Name	Z ($Z_\odot$)	$M_{\rm PAH}$ ($M_\odot$)	f_+	$M_{\rm dust}$ ($M_\odot$)	$L^{\rm dust}$ ($10^8\ L_\odot$)	$L^\star$ ($10^8\ L_\odot$)	Λ (g cm^{-2})	$\Lambda_{\rm MIR}$ (g cm^{-2})
M 83	$2.3^{+0.6}_{-0.5}$	$2.2^{+1.2}_{-1.8} \times 10^6$	$45 \pm 1\%$	$1.7^{+0.7}_{-0.5} \times 10^7$	226^{+13}_{-14}	380^{+80}_{-60}	$8.5^{+32.9}_{-0.6} \times 10^{-5}$	$1.5^{+1.0}_{-0.6} \times 10^{-4}$

Note. — Most of these quantities are defined in §3.2 and 3.3. $M_{\rm PAH}$ is the total mass of PAHs (Eq. 13); f_+ is the mass fraction of cationic PAHs (Eq. 13); $M_{\rm dust}$ is the mass of dust dominating the far-IR regime (Eq. 11); $L^{\rm dust}$ is the bolometric luminosity emitted by the dust; $L^{\rm star}$ is the intrinsic bolometric luminosity emitted by the stars. The sources are ordered according to their metallicity. The symbol $^{(?)}$ identifies uncertain values.

where $Z_{\rm gas}(t)$ is the metal-to-gas mass ratio, and $Z_{\rm dust}(t)$, the dust-to-gas mass ratio that will be discussed at §4.2.2. Its evolution is analog to Eq. (21):

$$\frac{{\rm d}\left[\Sigma_{\rm gas}(t)\, Z_{\rm ISM}(t)\right]}{{\rm d}t} = -Z_{\rm ISM}(t)\, \Sigma_{\rm SFR}(t) + \int_{m_l}^{m_u} \Sigma_{\rm SFR}(t-\tau(m))\, \frac{Y_{\rm Z}(m)}{\langle m \rangle}\, \phi(m)\, {\rm d}m, \qquad (23)$$

where $Y_Z(m)$ is the yield of elements heavier than He, by the stars of mass $[m, m+{\rm d}m]$.

The elemental yields, $Y_Z(m)$, for the low mass stars ($m \leq 8\ M_\odot$) are taken from Karakas & Lattanzio (2003a,b), and from Woosley & Weaver (1995) for the high mass stars ($m > 8\ M_\odot$). Furthermore, a prescription for the star formation rate is required, in order to solve these equations. This prescription is given by the Schmidt (1959) law, with the coefficients derived by Kennicutt (1998):

$$\frac{\Sigma_{\rm SFR}(t)}{1\ M_\odot\,{\rm yr}^{-1}\,{\rm pc}^{-2}} = (2.5 \pm 0.7) \times 10^{-10} \left(\frac{\Sigma_{\rm gas}(t)}{1\ M_\odot\,{\rm pc}^{-2}}\right)^{1.40\pm0.15} \qquad (24)$$

and is used to replace $\Sigma_{\rm SFR}(t)$ in Eq. (21). Fig. 16 shows the evolution of the total metallicity, and of the reduced gas mass $\mu_{\rm gas}(t) \equiv \Sigma_{\rm gas}(t)/\Sigma^0_{\rm gas}$, where $\Sigma^0_{\rm gas} = \Sigma_{\rm gas}(0)$ is the initial gas mass surface density.

4.2.2. Dust Formation and Destruction

The evolution of the mass surface density, $\Sigma_i(t)$, of a given dust specie, is the sum of three contributions: *(i)* the rate of dust destruction by star formation, *(ii)* the rate of dust condensation in stellar progenitors, *(iii)* the rate of dust destruction in the ISM, by SN blast waves:

$$\frac{{\rm d}\Sigma_{\rm i}(t)}{{\rm d}t} = -Z_{\rm i}(t)\, \Sigma_{\rm SFR}(t) + \int_{m_l}^{m_u} \frac{Y_{\rm i}(m)}{\langle m \rangle}\, \Sigma_{\rm SFR}(t-\tau(m))\, \phi(m)\, {\rm d}m - \frac{\Sigma_{\rm i}(t)}{\tau_{\rm dust}(t)}, \qquad (25)$$

where $Y_{\rm i}(m)$ is the yield of the considered dust specie by stars of mass $[m, m+{\rm d}m]$, and $\tau_{\rm dust}(t)$, the dust lifetime in the ISM.

The dust yields are derived from the elemental stellar yields described at §4.2.1, following Dwek (1998). For low mass stars ($m \leq 8\ M_\odot$), the dust yields depend on the value of the C/O ratio. We assume that the ejecta is microscopically mixed, so that all the excess carbon is locked-up in dust, if C>O. If C<O, then we combine all the available Fe, Si, Mg, Ca and Ti, with one O atom to produce silicate dust, and titanium oxydes. For high mass stars ($m > 8\ M_\odot$), we assume that the ejecta is only macroscopically mixed, so that both carbon and oxygen rich dust can condense. We assume a condensation efficiency of unity for all dust species.

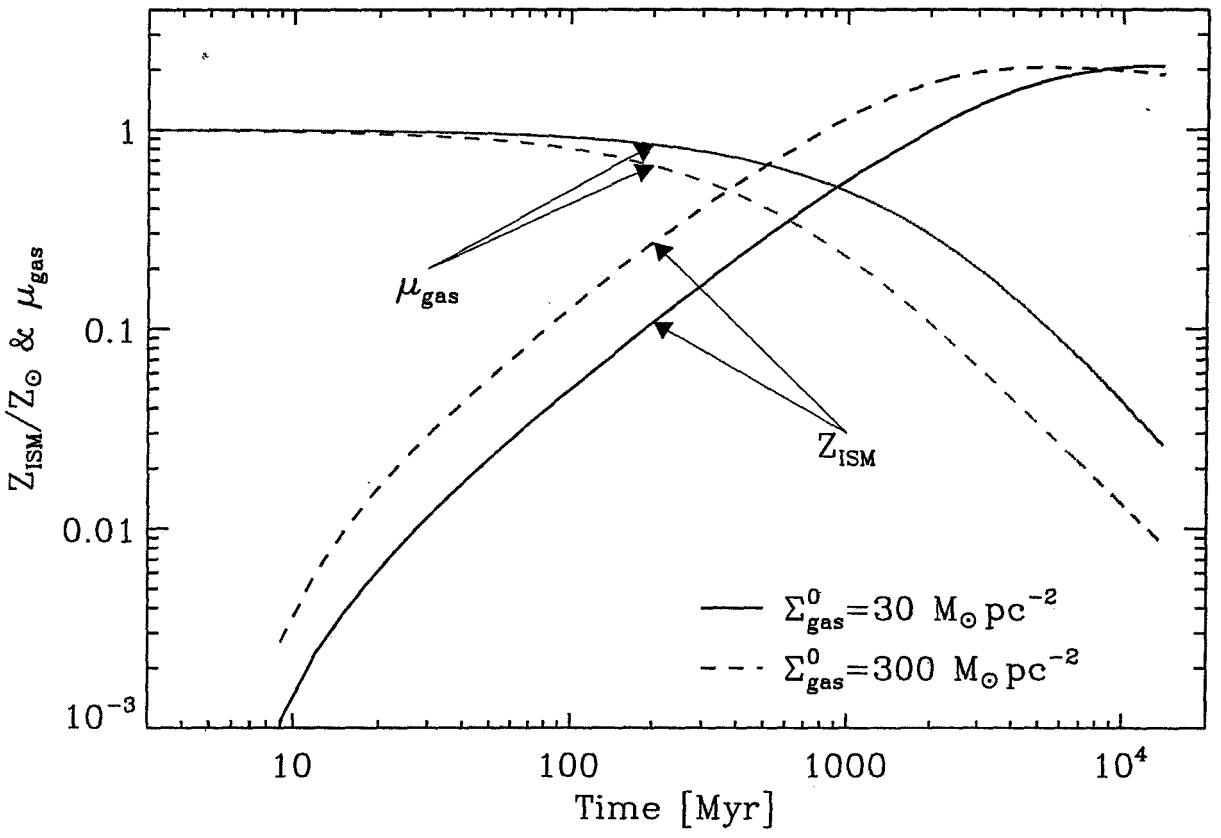

Fig. 16.— Evolution of the total metallicity (in units of $Z_\odot$), and of the reduced gas mass (μ_{gas}), for two different initial surface gas mass densities, Σ^0_{gas}.

The lifetime of dust, $\tau_{\rm dust}(t)$ is directly related to the SN II rate (Dwek & Scalo 1980; McKee 1986):

$$\tau_{\rm dust}(t) = \frac{\Sigma_{\rm gas}(t)}{R_{\rm SN\ II}(t)\ \langle m_{\rm ISM}\rangle}, \tag{26}$$

where $R_{\rm SN\ II}(t)$ is the SN II rate per unit area, and $\langle m_{\rm ISM}\rangle$ is the average effective mass of gas, swept up by a single SN remnant, where the dust is returned back to the gas phase, by either thermal sputtering, or grain-grain collision (Jones et al. 1996). The value of $\langle m_{\rm ISM}\rangle$ is largely unknown. We explore its effects, by varying it from $\langle m_{\rm ISM}\rangle = 0\ M_\odot$ (no destruction), to $\langle m_{\rm ISM}\rangle = 300\ M_\odot$ (typical destruction). The latter value is typical of our Galaxy. Indeed, if $M_{\rm gas}^{\rm Gal} \simeq 5\times10^9\ M_\odot$ is the total mass of gas in our Galaxy, $R_{\rm SN}^{\rm Gal} \simeq 1/30\ {\rm yr}^{-1}$, its average SN rate, and $\tau_{\rm dust}^{\rm Gal} \simeq 5\times10^8$ yr, the mean lifetime of an ISM dust particle (Jones 2004), then:

$$\langle m_{\rm ISM}\rangle \simeq \frac{M_{\rm gas}^{\rm Gal}}{R_{\rm SN}^{\rm Gal}\ \tau_{\rm dust}^{\rm Gal}} \simeq 300\ M_\odot. \tag{27}$$

Fig. 17 shows the evolution of the total dust content formed by massive stars, and the carbon dust formed by AGB stars, for various initial conditions, and destruction efficiencies. The SN II dust evolves almost linearly with the metallicity, in absence of destruction, because the metal enrichment is dominated by massive stars. In contrast, the AGB carbon dust starts rising when the metallicity of the ISM is around $1/20\ Z_\odot$. This value corresponds to a time of ~ 100 Myr (Fig. 16), which the lifetime of the most massive AGB stars. Hence, the carbon dust produced by AGB stars is injected into the ISM, with a delay which corresponds to the lifetime of the stars. **This evolutionary trend was previously noted by Dwek (1998) and Morgan & Edmunds (2003).** The change in the slope of the AGB carbon dust, around $1\ Z_\odot$, is simply due to the fact that AGB stars of lifetime longer than ~ 1 Gyr are oxygen rich. The dust destruction effects the evolution for $Z \gtrsim 0.1\ Z_\odot$.

4.3. PAHs and the Delayed Injection of AGB Carbon Dust

From an observational point of view, PAHs are believed to form in the circumstellar enveloppes of carbon rich AGB stars, and to be subsequently ejected into the ISM through stellar winds. However, the direct indications of this formation process, on individual stars are very few (Hony et al. 2001; Boersma et al. 2006). The main reason for this lack of observational evidence, is probably that the PAHs are not sufficiently excited by their UV deficient stellar progenitor. **In what follows, we will assume that PAHs are only formed in the envelopes of AGB stars.**

Fig. 18 shows the comparison between the dust and PAH abundances derived from the observations (Fig. 15), and the ones produced by the evolution model (Fig. 17). The

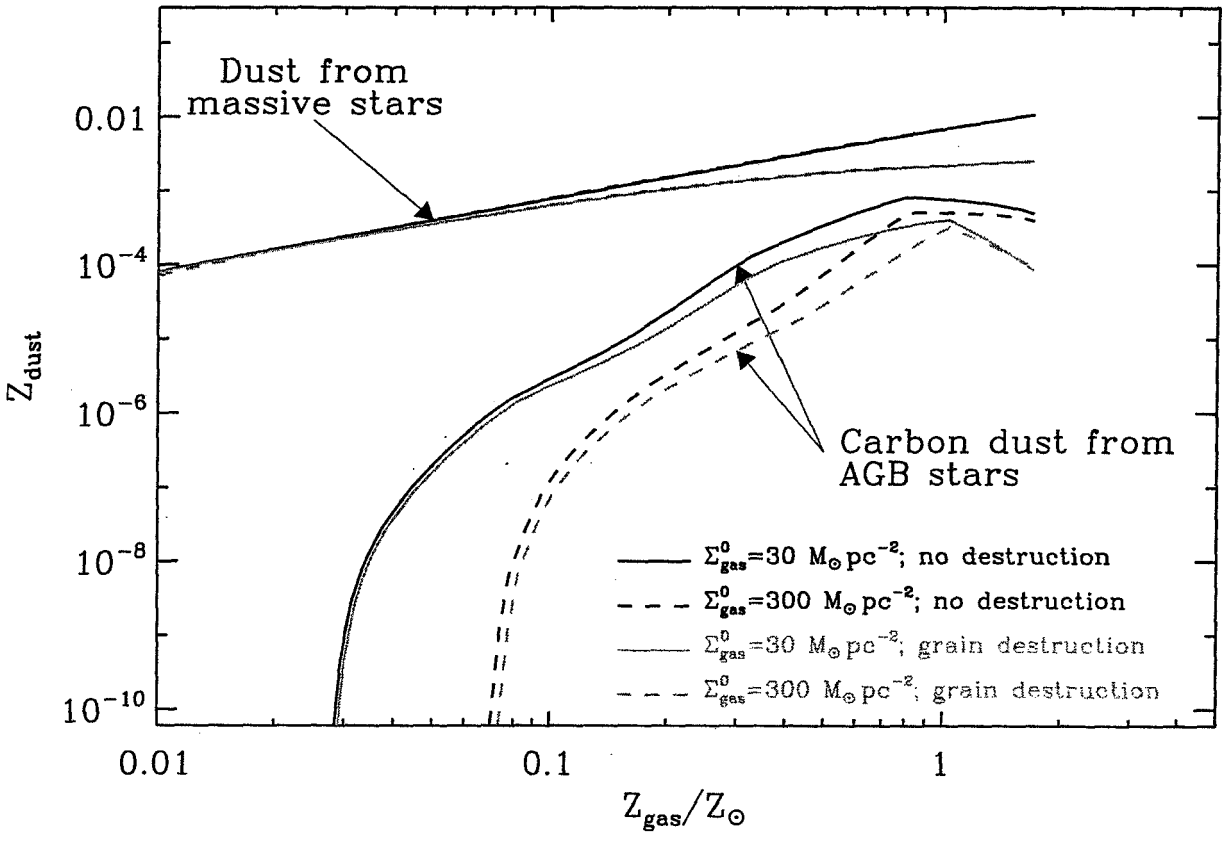

Fig. 17.— Evolution of the dust content with the metallicity of the ISM. We adopt $\langle m_{\rm ISM} \rangle = 300\ M_\odot$, for the curves with grain destruction.

agreement between the PAH-to-gas mass ratio, and the carbon dust production by AGB stars is very good. Hence, the peculiar evolution of the PAH content in galaxies can naturally be explained by the delayed injection of carbon dust into the ISM, by AGB stars.

The galaxy He 2-10 is the only outlier. This object is a solar metallicity blue compact dwarf galaxy. Its SED is similar to lower metallicity galaxies (Galliano et al. 2005), however its metallicity is very uncertain; for example Vacca & Conti (1992) quoted 1/6 $Z_{\odot}$. This uncertainty may reside in the fact that this galaxy has two cores, resulting from a merger. The properties of these nuclei are different in terms of dust absorption (Phillips et al. 1984), molecular gas content (Baas et al. 1994), compact source distribution (Cabanac et al. 2005), and mid-IR spectrum (Martín-Hernández et al. 2006). Thus, our global approach may not apply to this object.

Two processes, that were not taken into account in our model, may potentially have an impact on the observed trend of PAH abundance with metallicity: *(i)* an additional, non-AGB, source of PAHs, and *(ii)* a radiative destruction mechanism, in addition to the mechanical one by SNRs. We argue below, that none of these processes will affect the observed trend of PAHs with metallicity.

In principle, PAHs can form by some interstellar processes, for example, by the hydrogenation of small carbon grains. Initially, their abundance will then follow the evolutionary trend of SN-condensed carbon dust. However, their absence in low metallicity systems suggests that they are efficiently destroyed, presumably by shocks or UV radiation, as envisioned in by Madden et al. (2006) or O'Halloran et al. (2006). At later times, the rate of PAH production by these interstellar processes will follow the evolutionary trend of AGB stars, since they will be the major source of carbon dust in the ISM.

Our model ignored the destruction of PAHs by UV photons capable of subliming or dissociating these molecules. However, since all hard UV photons are produced by massive stars that eventually become SN, the PAH destruction rate by UV radiation will follow the same time dependence as their destruction rate by SNR. The main difference between the two destruction mechanisms is that the PAH destruction efficiency by UV radiatin will be more efficient at earlier times, when the dust abundance is low and the ISM more transparent to UV radiation. The main effect of the UV radiation will therefore be to destroy any PAHs that may have formed at early times by non-AGB sources. At later times, the effect of UV destruction will mainly effect the model by increasing the value of $\langle m_{\rm ISM} \rangle$, which will now include the effective mass of the ISM gas that was cleared of PAHs by UV radiation, in addition to that cleared by shocks.

In summary, at early times the two processes discussed above cancel each other out, since the UV radiation can effectively destroy most of the PAHs that may have formed by interstellar processes before the first progenitors of AGB stars evolved off the main sequence. At later times, the two processes will be indistinguishable from those already considered in the paper: any interstellar PAH source will follow the time evolution of AGB stars, and any UV destruction mechansim will follow that of the destruction rate by SNRs.

The global trend of PAH abundance with metallicity does not preclude the possibility of local variations of PAH abundance in individual galaxies. For example, the SMC which has on the average a metallicity that is 1/6 $Z_\odot$ (Dufour et al. 1982) has at least one region, the molecular cloud SMC B1#1 (Reach et al. 2000), with a PAH-to-dust ratio that is comparable to the Galactic value (Li & Draine 2002). Even in our Galaxy, there are regions with "super Galactic" PAH abundances (e.g. Ridderstad et al. 2006). Such local abundance variations are a natural consequences of processes, such as mixing of stellar ejecta and cycling between the ISM phases, that when globally averaged, will follow the general trend of PAH abundances with metallicity depicted in Fig. 18.

4.4. The Evolutionary Trend of SN-Condensed Dust

The far-IR dust content is in good agreement with the dust production by SN II, down to $\sim 0.1\ Z_\odot$ (Fig. 18). Below this value, the model systematically overestimates the observed far-IR dust content. There may be several reasons for this discrepancy.

First, we may have overestimated the gas mass, in the lowest metallicity sources. Indeed, the distribution of H I of these galaxies extends farther out of the star forming region, as discussed in §4.1. We have attempted to correct this effect, for I Zw 18 and SBS 0335-052, by considering only the gas content associated with the optical galaxy. However, we could not correct for the gas located out of the star forming region and along the line of sight.

Second, we may have underestimated the dust mass by overlooking a cold dust component. Indeed, Galliano et al. (2003, 2005) showed that the submillimetre excess observed in the SEDs of NGC 1140, NGC 1569, II Zw 40, and He 2-10, could be consistently explained by the presence of very cold dust, accounting for 40 to 80% of the total dust mass. On Fig. 18, the FIR-dust-to-gas mass ratio of these four galaxies is indeed, below the SN II production rate by a factor of ~ 2. Assuming that the high clumpiness of the ISM is a general property of low-metallicity systems, and that the filling factor and/or contrast den-

sity of these clumps rises when the metallicity drops, we have a natural explanation for this deviation. We can not address this issue, because of the lack of submillimetre data for these very low-metallicity galaxies.

Third, the discrepancy between the predicted and observed SN II dust at low metallicity could be due to several parameters or assumptions used in the chemical evolution modeling. (1) The IMF could play an important role in the absolute value of the dust production by SN II. It would indicate that the slope of the IMF is metallicity-dependent, and that the contribution of massive stars is lower, at very low $Z_{\rm ISM}$, which seems to be unlikely, both from a theoretical point of view (star formation), and an observational point of view (star counts). (2) A much more likely explanation could come from the fact that we assumed that the condensation into dust of the elements ejected by the SN II and their mixing in the ISM is instantaneous. If the major part of the dust was to condense into the ISM, and not directly into the SN II-ejecta, then the dust formation would be delayed after the death of the massive stars. (3) Finally, the dust production rates, computed from our dust evolution model, implicitely assume that the star formation rate of the galaxy is smooth and that the mixing is instantaneous. This hypothesis is certainly valid for evolved systems, but could be wrong for very young objects. For example, Legrand et al. (2000) suggested that the star formation history of I Zw 18 is not continuous.

5. CONCLUSION AND SUMMARY

The origin of the weakness of the mid-IR aromatic features – commonly attributed to emission from PAHs – in low-metallicity environments has been traditionally interpreted as the consequence of the increased selective destruction efficiency of the PAHs in these environments. In this paper, we presented a new interpretation for the observed correlation of the intensity of the mid-IR emission from PAHs with galaxies' metallicity. In our model, the trend is a manifestation of the evolution of the abundance of PAHs that condensed in AGB stars. **We also show that the inclusions of any source of PAHs, in addition to the AGB stars considered here, and a radiative destruction mechanism, in addition to the mechanical one by SNRs, will still retain the evolutionary trend of AGB condensed dust abundance with metallicity.**

To ascertain this trend and derive the abundance of PAHs, we modeled the UV to far-IR SEDs in a sample of 35 nearby galaxies, with metallicities ranging from 1/50 to $\sim 3\ Z_{\odot}$. From these models, we determined the intrinsic stellar radiation field which was used to determine the abundance of the PAHs giving rise to the mid-IR aromatic features, and the abundance of the dust that gives rise to the far-IR emission. We then used a chemical

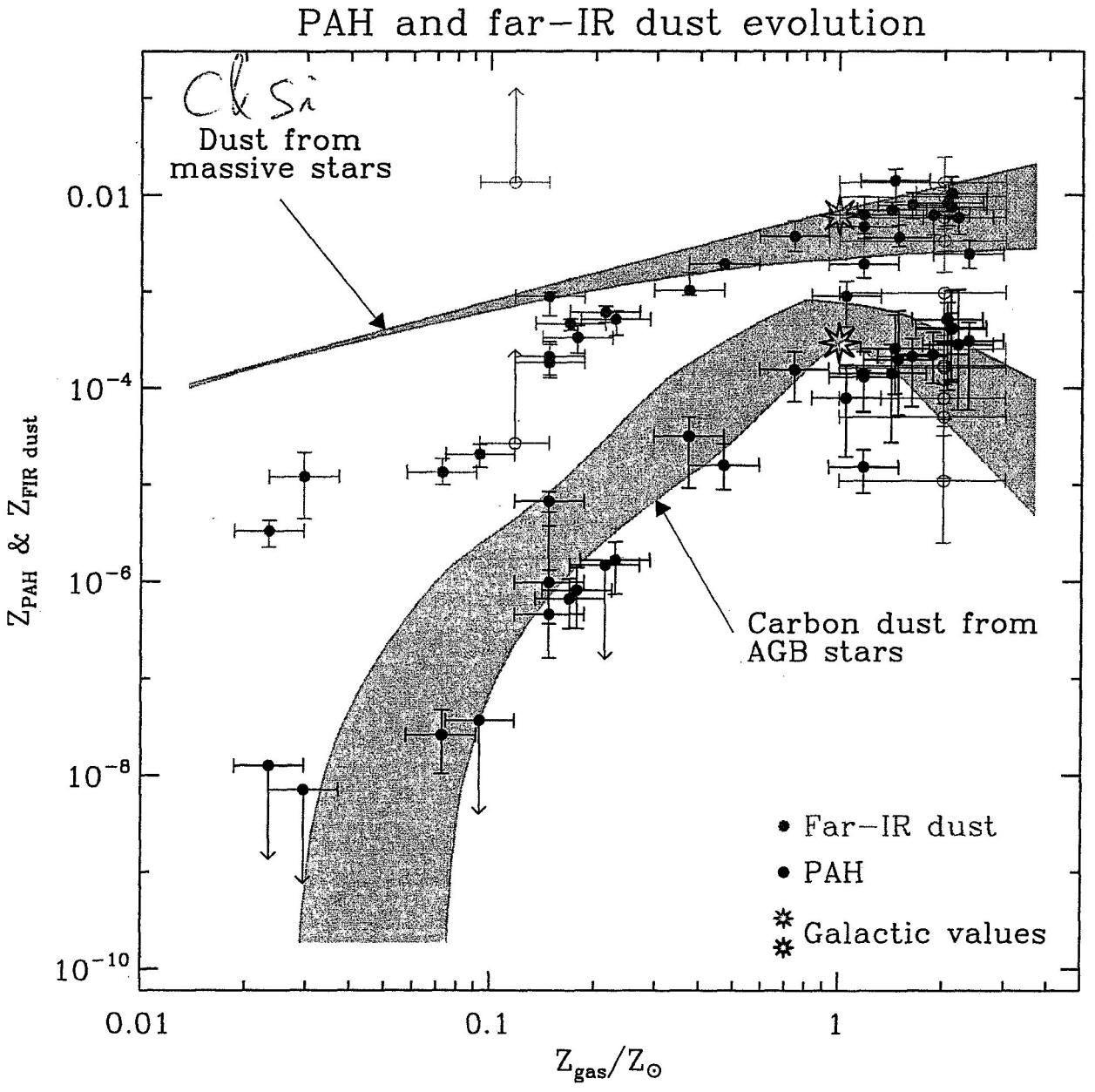

Fig. 18.— Comparison between the metallicity trends of the PAH abundance derived from the observed SED and those derived from the chemical evolution model. The figure highlights the different evolutionary trend of SN II- and AGB-condensed dust.

evolution model to calculate the abundances of SN- and AGB-condensed dust as a function of time – or metallicity. The model takes into account the delayed recycling of the ejecta from low-mass stars caused by their finite main-sequence lifetime.

The main conclusions of this paper are the followings.

1. In our analysis of the mid-IR spectra of nearby galaxies, we detected the 7.7 μm aromatic feature at the 4σ level in VII Zw 403, a dwarf galaxy with $Z \simeq 1/20\ Z_{\odot}$. This is the lowest metallicity galaxy for which PAH emission has been detected to date.

2. We find that the derived relative abundance of PAHs and FIR-dust evolves with metallicity, suggesting distinct evolutionary histories for these two types of dust grains.

3. Comparison of the observed dust-to-gas mass ratios with the results of our chemical evolution model shows the following: (1) the delayed injection of PAHs into the ISM provides a natural explanation for the paucity of these large molecules in low metallicity systems; (2) the subsequent rise in the PAH-to-gas mass ratio with metallicity is then a natural consequence of the increasing contribution of AGB stars to the chemical enrichment of the ISM as they evolve off the main sequence; (3) the evolutionary trend of FIR-dust-to-gas mass ratio with metallicity generally follows the distinct evolution of SN-condensed dust which is instantaneously injected into the ISM after the birth of the progenitor star.

4. The inferred FIR-dust-to-gas mass ratio falls below the calculated value for SN-condense dust in the lowest metallicity galaxies. This discrepancy may be due to one or more of the following: (1) an overestimate of the H I gas mass used to derive this dust-to-gas mass ratio; (2) an underestimate of the FIR-dust mass due to the possible presence of a cold dust component; (3) the gradual mixing of SN ejecta into the ambient medium; and finally (4) a more complex star formation history than used in the model calculations.

The success of our chemical evolution model, in reproducing the trend of PAH abundances with metallicity, strongly suggests the importance of stellar evolutionary effects in determining the abundances and composition of dust in galaxies. These will have important consequences for the opacity of galaxies and their reradiated thermal IR emission. Chemical evolution models for dust must therefore be an integral part of population synthesis models, providing a self-consistent link between the stellar and dust emission components of the SED of galaxies.

We thank Els Peeters for her expert advices on the IRS spectra extraction. We are grateful to Sacha Hony for a useful discussion about AGB stars. This work was performed while two of us (F. G. & P. C.) held a National Research Council/Oak Ridge Associated Universities research associateship award at NASA Goddard Space Flight Center. E. D. acknowledges the support of NASA's LTSA03-0000-065. This study is based in part on observations with *ISO*, an ESA project with instruments funded by ESA Member States (especially the PI countries: France, Germany, the Netherlands and the United Kingdom) and with the participation of ISAS and NASA. This work is also based in part on observations made with the *Spitzer Space Telescope*, which is operated by the Jet Propulsion Laboratory, California Institute of Technology under a contract with NASA. This research has made use of the HYPERLEDA database (http://leda.univ-lyon1.fr) and of the NASA/IPAC Extragalactic Database (NED) which is also operated by the Jet Propulsion Laboratory, California Institute of Technology, under contract with the National Aeronautics and Space Administration.

REFERENCES

Allamandola, L. J., Tielens, A. G. G. M., & Barker, J. R. 1985, ApJ, 290, L25

Alloin, D., Collin-Souffrin, S., Joly, M., & Vigroux, L. 1979, A&A, 78, 200

Appleton, P. N., Davies, R. D., & Stephenson, R. J. 1981, MNRAS, 195, 327

Baas, F., Israel, F. P., & Koornneef, J. 1994, A&A, 284, 403

Bakes, E. L. O. & Tielens, A. G. G. M. 1994, ApJ, 427, 822

Bergvall, N., Masegosa, J., Östlin, G., & Cernicharo, J. 2000, A&A, 359, 41

Bernloehr, K. 1993, A&A, 270, 20

Bettoni, D., Galletta, G., & García-Burillo, S. 2003, A&A, 405, 5

Biviano, A., Sauvage, M., Gallais, P., et al. 1998, The ISOCAM dark current calibration report, Tech. rep., ESA/ISO Data Centre

Boersma, C., Hony, S., & Tielens, A. G. G. M. 2006, A&A, 447, 213

Boomsma, R., Oosterloo, T. A., Fraternali, F., van der Hulst, J. M., & Sancisi, R. 2005, A&A, 431, 65

Boselli, A., Lequeux, J., & Gavazzi, G. 2002, A&A, 384, 33

Brandl, B. R., Devost, D., Higdon, S. J. U., et al. 2004, ApJS, 154, 188

Bresolin, F., Garnett, D. R., & Kennicutt, Jr., R. C. 2004, ApJ, 615, 228

Cabanac, R. A., Vanzi, L., & Sauvage, M. 2005, ApJ, 631, 252

Carignan, C., Charbonneau, P., Boulanger, F., & Viallefond, F. 1990, A&A, 234, 43

Casasola, V., Bettoni, D., & Galletta, G. 2004, A&A, 422, 941

Cesarsky, C. J., Abergel, A., Agnese, P., et al. 1996a, A&A, 315, L32

Cesarsky, D., Lequeux, J., Abergel, A., et al. 1996b, A&A, 315, L309

Chanial, P. 2003, PhD thesis, University of Paris VII

Coulais, A. & Abergel, A. 2000, A&AS, 141, 533

Crowther, P. A., Beck, S. C., Willis, A. J., et al. 1999, MNRAS, 304, 654

Dahlem, M., Aalto, S., Klein, U., et al. 1990, A&A, 240, 237

Dahlem, M., Ehle, M., & Ryder, S. D. 2001, A&A, 373, 485

Dahlem, M., Golla, G., Whiteoak, J. B., et al. 1993, A&A, 270, 29

Dale, D. A., Bendo, G. J., Engelbracht, C. W., et al. 2005, ApJ, 633, 857

Dean, J. F. & Davies, R. D. 1975, MNRAS, 170, 503

Désert, F.-X., Boulanger, F., & Puget, J. L. 1990, A&A, 237, 215

Draine, B. T. & Li, A. 2001, ApJ, 551, 807

Dufour, R. J., Shields, G. A., & Talbot, Jr., R. J. 1982, ApJ, 252, 461

Durret, F., Bergeron, J., & Boksenberg, A. 1985, A&A, 143, 347

Dutil, Y. & Roy, J.-R. 1999, ApJ, 516, 62

Dwek, E. 1998, ApJ, 501, 643

Dwek, E. 2005, in AIP Conf. Proc. 761: The Spectral Energy Distributions of Gas-Rich Galaxies: Confronting Models with Data, ed. C. C. Popescu & R. J. Tuffs, 103

Dwek, E., Arendt, R. G., Fixsen, D. J., et al. 1997, ApJ, 475, 565

Dwek, E., Fioc, M., & Varosi, F. 2000, in LNP Vol. 548: ISO Survey of a Dusty Universe, ed. D. Lemke, M. Stickel, & K. Wilke, 157–+

Dwek, E., Galliano, F., & Jones, A. P. 2007, ApJ accepted

Dwek, E. & Scalo, J. M. 1980, ApJ, 239, 193

Elmouttie, M., Krause, M., Haynes, R. F., & Jones, K. L. 1998, MNRAS, 300, 1119

Engelbracht, C. W., Gordon, K. D., Rieke, G. H., et al. 2005, ApJ, 628, L29

Fioc, M. & Rocca-Volmerange, B. 1997, A&A, 326, 950

Gallais, P., Charmandaris, V., Le Floc'h, E., et al. 2004, A&A, 414, 845

Galliano, F., Madden, S. C., Jones, A. P., Wilson, C. D., & Bernard, J.-P. 2005, A&A, 434, 867

Galliano, F., Madden, S. C., Jones, A. P., et al. 2003, A&A, 407, 159

Galliano, F., Madden, S. C., Tielens, A. G. G. M., et al. 2007, ApJ to be submitted

Gerin, M., Combes, F., & Nakai, N. 1988, A&A, 203, 44

Gonzalez-Delgado, R. M., Perez, E., Diaz, A. I., et al. 1995, ApJ, 439, 604

Grevesse, N. & Sauval, A. J. 1998, Space Science Reviews, 85, 161

Haas, M., Klaas, U., & Bianchi, S. 2002, A&A, 385, L23

Heckman, T. M., Robert, C., Leitherer, C., Garnett, D. R., & van der Rydt, F. 1998, ApJ, 503, 646

Helfer, T. T., Thornley, M. D., Regan, M. W., et al. 2003, ApJS, 145, 259

Higdon, S. J. U., Devost, D., Higdon, J. L., et al. 2004, PASP, 116, 975

Hony, S., Van Kerckhoven, C., Peeters, E., et al. 2001, A&A, 370, 1030

Hopkins, A. M., Schulte-Ladbeck, R. E., & Drozdovsky, I. O. 2002, AJ, 124, 862

Houck, J. R., Charmandaris, V., Brandl, B. R., et al. 2004a, ApJS, 154, 211

Houck, J. R., Roellig, T. L., van Cleve, J., et al. 2004b, ApJS, 154, 18

Houghton, S., Whiteoak. J. B., Koribalski, B., et al. 1997, A&A, 325, 923

Huchtmeier, W. K. & Richter, O.-G. 1988, A&A, 203, 237

Hunt, L., Bianchi, S., & Maiolino, R. 2005, A&A, 434, 849

Hunter, D. A., van Woerden, H., & Gallagher, III, J. S. 1994, ApJS, 91, 79

Israel, F. P. 1997, A&A, 328, 471

Israel, F. P. 2005, A&A, 438, 855

Izotov, Y. I., Chaffee, F. H., Foltz, C. B., et al. 1999, ApJ, 527, 757

Izotov, Y. I. & Thuan, T. X. 1998, ApJ, 500, 188

Jarrett, T. H., Chester, T., Cutri, R., Schneider, S. E., & Huchra, J. P. 2003, AJ, 125, 525

Jones, A. P. 2004, in ASP Conf. Ser. 309: Astrophysics of Dust, ed. A. N. Witt, G. C. Clayton, & B. T. Draine, 347

Jones, A. P., Tielens, A. G. G. M., & Hollenbach, D. J. 1996, ApJ, 469, 740

Jorsater, S. & van Moorsel, G. A. 1995, AJ, 110, 2037

Karakas, A. I. & Lattanzio, J. C. 2003a, Publications of the Astronomical Society of Australia, 20, 393

Karakas, A. I. & Lattanzio, J. C. 2003b, Publications of the Astronomical Society of Australia, 20, 279

Kennicutt, Jr., R. C. 1998, ApJ, 498, 541

Kessler, M. F., Steinz, J. A., Anderegg, M. E., et al. 1996, A&A, 315, L27

Kobulnicky, H. A., Kennicutt, Jr., R. C., & Pizagno, J. L. 1999, ApJ, 514, 544

Kobulnicky, H. A. & Skillman, E. D. 1997, ApJ, 489, 636

Kunth, D. & Joubert, M. 1985, A&A, 142, 411

Laor, A. & Draine, B. T. 1993, ApJ, 402, 441

Laurent, O., Mirabel, I. F., Charmandaris, V., et al. 2000, A&A, 359, 887

Léger, A. & Puget, J. L. 1984, A&A, 137, L5

Legrand, F., Kunth, D., Roy, J.-R., Mas-Hesse, J. M., & Walsh, J. R. 2000, A&A, 355, 891

Li, A. & Draine, B. T. 2001, ApJ, 554, 778

Li, A. & Draine, B. T. 2002, ApJ, 576, 762

Lundgren, A. A., Wiklind, T., Olofsson, H., & Rydbeck, G. 2004, A&A, 413, 505

Madden, S. C., Galliano, F., Jones, A. P., & Sauvage, M. 2006, A&A, 446, 877

Martín-Hernández, N. L., Peeters, E., Morisset, C., et al. 2002, A&A, 381, 606

Martín-Hernández, N. L., Schaerer, D., Peeters, E., Tielens, A. G. G. M., & Sauvage, M. 2006, A&A, 455, 853

Mas-Hesse, J. M. & Kunth, D. 1999, A&A, 349, 765

Mattioda, A. L., Hudgins, D. M., & Allamandola, L. J. 2005, ApJ, 629, 1188

McKee, C. F. 1986, Ap&SS, 118, 383

Meier, D. S., Turner, J. L., & Beck, S. C. 2002, AJ, 124, 877

Morgan, H. L. & Edmunds, M. G. 2003, MNRAS, 343, 427

Moshir, M. & et al. 1990, in IRAS Faint Source Catalogue, version 2.0 (1990), 0

O'Halloran, B., Satyapal, S., & Dudik, R. P. 2006, ApJ, 641, 795

Ondrechen, M. P. & van der Hulst, J. M. 1989, ApJ, 342, 29

Otte, B., Reynolds, R. J., Gallagher, III, J. S., & Ferguson, A. M. N. 2001, ApJ, 560, 207

Paturel, G., Theureau, G., Bottinelli, L., et al. 2003, A&A, 412, 57

Peeters, E., Martín-Hernández, N. L., Damour, F., et al. 2002, A&A, 381, 571

Pei, Y. C. 1992, ApJ, 395, 130

Pérez-Montero, E. & Díaz, A. I. 2003, MNRAS, 346, 105

Phillips, M. M., Aitken, D. K., & Roche, P. F. 1984, MNRAS, 207, 25

Pilyugin, L. S., Vílchez, J. M., & Contini, T. 2004, A&A, 425, 849

Plante, S. & Sauvage, M. 2002, AJ, 124, 1995

Pustilnik, S. A., Brinks, E., Thuan, T. X., Lipovetsky, V. A., & Izotov, Y. I. 2001, AJ, 121, 1413

Ravindranath, S. & Prabhu, T. P. 2001, Ap&SS, 276, 593

Reach, W. T., Boulanger, F., Contursi, A., & Lequeux, J. 2000, A&A, 361, 895

Reach, W. T., Rho, J., Jarrett, T. H., & Lagage, P.-O. 2002, ApJ, 564, 302

Reif, K., Mebold, U., Goss, W. M., van Woerden, H., & Siegman, B. 1982, A&AS, 50, 451

Rice, W., Lonsdale, C. J., Soifer, B. T., et al. 1988, ApJS, 68, 91

Richter, O.-G., Sackett, P. D., & Sparke, L. S. 1994, AJ, 107, 99

Ridderstad, M., Juvela, M., Lehtinen, K., Lemke, D., & Liljeström, T. 2006, A&A, 451, 961

Roussel, H., Vigroux, L., Bosma, A., et al. 2001, A&A, 369, 473

Roy, J.-R. & Walsh, J. R. 1997, MNRAS, 288, 715

Sage, L. J., Salzer, J. J., Loose, H.-H., & Henkel, C. 1992, A&A, 265, 19

Sanders, D. B., Scoville, N. Z., & Soifer, B. T. 1991, ApJ, 370, 158

Sandqvist, A., Joersaeter, S., & Lindblad, P. O. 1995, A&A, 295, 585

Sargent, A. I., Sanders, D. B., & Phillips, T. G. 1989, ApJ, 346, L9

Sauvage, M., Thuan, T. X., & Lagage, P. O. 1997, A&A, 325, 98

Schaerer, D., Guseva, N. G., Izotov, Y. I., & Thuan, T. X. 2000, A&A, 362, 53

Schlegel, D. J., Finkbeiner, D. P., & Davis, M. 1998, ApJ, 500, 525

Schmidt, M. 1959, ApJ, 129, 243

Spoon, H. W. W., Moorwood, A. F. M., Lutz, D., et al. 2004, A&A, 414, 873

Starck, J. L., Abergel, A., Aussel, H., et al. 1999, A&AS, 134, 135

Staveley-Smith, L. & Davies, R. D. 1987, MNRAS, 224, 953

Stil, J. M. & Israel, F. P. 2002, A&A, 392, 473

Storchi-Bergmann, T., Kinney, A. L., & Challis, P. 1995, ApJS, 98, 103

Struck, C. & Smith, B. J. 2003, ApJ, 589, 157

Tacconi, L. J. & Young, J. S. 1986, ApJ, 308, 600

Thuan, T. X., Hibbard, J. E., & Lévrier, F. 2004, AJ, 128, 617

Thuan, T. X., Lipovetsky, V. A., Martin, J.-M., & Pustilnik, S. A. 1999a, A&AS, 139, 1

Thuan, T. X. & Martin, G. E. 1981, ApJ, 247, 823

Thuan, T. X., Sauvage, M., & Madden, S. 1999b, ApJ, 516, 783

Tielens, A. G. G. M. & Hollenbach, D. 1985, ApJ, 291, 722

Tilanus, R. P. J. & Allen, R. J. 1993, A&A, 274, 707

Vacca, W. D. & Conti, P. S. 1992, ApJ, 401, 543

van Zee, L., Westpfahl, D., Haynes, M. P., & Salzer, J. J. 1998, AJ, 115, 1000

Vanzi, L. & Sauvage, M. 2004, A&A, 415, 509

Városi, F. & Dwek, E. 1999, ApJ, 523, 265

Vermeij, R., Peeters, E., Tielens, A. G. G. M., & van der Hulst, J. M. 2002, A&A, 382, 1042

Walter, F., Weiss, A., & Scoville, N. 2002, ApJ, 580, L21

Webster, B. L. & Smith, M. G. 1983, MNRAS, 204, 743

Weingartner, J. C. & Draine, B. T. 2001, ApJ, 548, 296

Werner, M. W., Roellig, T. L., Low, F. J., et al. 2004, ApJS, 154, 1

Wild, W., Eckart, A., & Wiklind, T. 1997, A&A, 322, 419

Woosley, S. E. & Weaver, T. A. 1995, ApJS, 101, 181

Wu, Y., Charmandaris, V., Hao, L., et al. 2006, ApJ, 639, 157

Xilouris, E. M., Madden, S. C., Galliano, F., Vigroux, L., & Sauvage, M. 2004, A&A, 416, 41

Yun, M. S. & Hibbard, J. E. 2001, ApJ, 550, 104

Zaritsky, D., Kennicutt, Jr., R. C., & Huchra, J. P. 1994, ApJ, 420, 87

Zubko, V., Dwek, E., & Arendt, R. G. 2004, ApJS, 152, 211